The Significance of the Dispersive Behavior of Left Ventricle Filling Waves

Casandra Leigh Niebel

Thesis submitted to the faculty of the Virginia Polytechnic Institute and State University
in partial fulfillment of the requirements for the degree of

Master of Science
In
Mechanical Engineering

Pavlos P. Vlachos
William Little
Wally Grant
Sungwan Jung

October 11, 2012
Blacksburg, VA

Keywords: Diastolic Dysfunction, Dispersive Waves, Wavelet Transform

The Significance of the Dispersive Behavior of Left Ventricle Filling Waves

Casandra Leigh Niebel

ABSTRACT

Left ventricular diastolic dysfunction (LVDD) is any abnormality in the filling of the left ventricle (LV). Despite the prevalence of this disease, it remains difficult to diagnose, mainly due to inherent compensatory mechanisms and a limited physical understanding of the filling process. LV filling can be non-invasively imaged using color m-mode echocardiography which provides a spatio-temporal map of inflow velocity. These filling patterns, or waves, are conventionally used to qualitatively assess the filling pattern, however, this work aims to physically quantify the filling waves to improve understanding of diastole and develop robust, reliable, and quantitative parameters.

This work reveals that LV filling waves in a normal ventricle act as dispersive waves and not only propagate along the length of the LV but also spread and disperse in the direction of the apex. In certain diseased ventricles, this dispersion is limited due to changes in LV geometry and wall motion. This improved understanding could aid LVDD diagnostics not only for determining health and disease, but also for distinguishing between progressing disease states.

This work also indentifies a limitation in a current LVDD parameter, intra ventricular pressure difference (IVPD), and presents a new methodology to address this limitation. This methodology is also capable of synthesizing velocity information from a series of heartbeats to generating one representative heartbeat, addressing inaccuracies due to beat-to-beat variations. This single beat gives a comprehensive picture of that specific patient's filling pattern. Together, these methods improve the clinical utility of IVPD, making it more robust and limiting the chance for a misdiagnosis.

Acknowledgements

I would like to thank all of the people who have helped me and supported me during my time at Virginia Tech. I would like to thank my committee members, Pavlos Vlachos, William Little, Wally Grant, and Sunny Jung for their help in advising me during this research project. I have thoroughly enjoyed working on such an interdisciplinary research project and have gained valuable experience and learned more than I could have imagined throughout this whole experience.

Pavlos encouraged me to apply for the National Science Foundation Graduate Research Fellowship and brought me into his lab to work on this unique project. Thank you for advising me and pushing me to produce high quality work.

I also want to thank William Little and Takahiro Ohara at the Wake Forest University Baptist Medical Center for their insight on the clinical aspect of this research and for all of the data they have collected. This research would not have been possible without them.

Also, I would like to thank the National Science Foundation for awarding me with this fellowship and for continuing to fund interdisciplinary research projects, many of which would not be possible without their support.

Thank you to my lab mates, past and present that have provided advice, help, Matlab codes, and sanity checks along the way. A special thanks to Kelley Stewart and John Charonko for setting the groundwork of this project for me to build from.

Finally, I must thank the people of most importance to me. To my family, thank you for always supporting me and encouraging me in all that I do. I would not be the person I am today if it were not for your constant love and support. Finally, to James Reed, thank you for always being there for me, I can't think of anyone better to have by my side.

Table of Contents

List of Figures

List of Tables

1. Introduction

1.1 Motivation

Despite increasing prevalence, left ventricular diastolic dysfunction (LVDD) remains difficult to diagnose. LVDD is any abnormality or impairment in the filling of the left ventricle (LV) and is present in 81% of patients with symptoms of systolic heart failure as shown in Figure 1.1. More importantly, studies have found that LVDD could affect nearly a third (28%) of the asymptomatic population (*1*, *2*). There is currently no diagnostic gold standard for LVDD, and because diastole is governed by many complex interrelated mechanisms such as LV pressures, left atrial pressures, LV recoil, myocardial compliance, and remodeling (*3*, *4*), developing a physics based diagnostic parameter relies on a strong physical understanding of these mechanisms and how they affect the filling process. Robust diagnostics are also dependent on repeatable, high resolution, and accurate measurements of the filling wave, which is currently limited for most pertinent imaging modalities.

The overarching motivation behind this work is to physically understand how blood enters to fill the LV. Understanding how the filling wave changes in health and disease and in various remodeled geometries can then be used to develop improved diagnostic parameters, which are physics based, robust and repeatable.

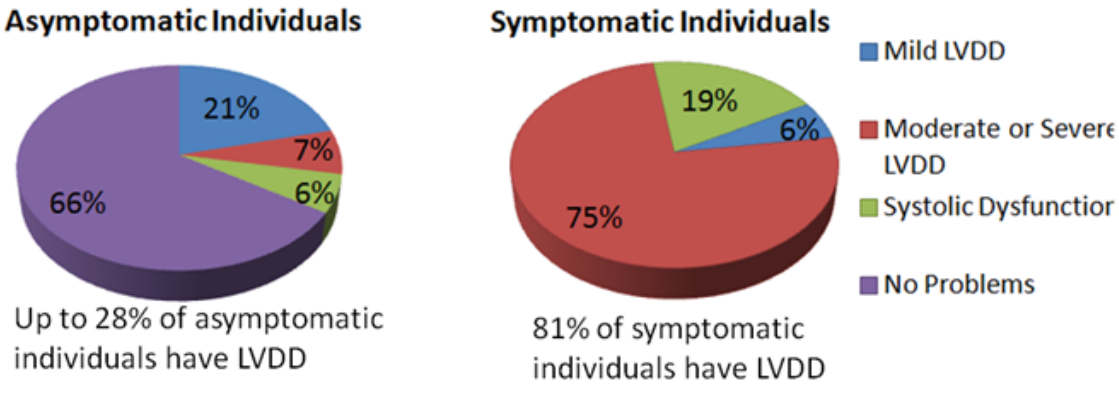

Figure 1.1: Prevalence of LVDD in Symptomatic and Asymptomatic individuals. 81% of patients with signs of heart failure also have diastolic dysfunction. Nearly a third (28%) of the asymptomatic population may have LVDD. Data from (*1*, *2*).

1.2 Background

1.2.1 Heart Failure and LV Remodeling

Heart failure alters the loading conditions on the heart. In response to an increased volume load or an increased pressure load, the LV must alter form and function to continue supplying oxygenated blood to the body (*5*, *6*). This remodeling process is not completely understood, but is most likely governed by cell signaling pathways which become altered in disease (*7*-*9*).

In response to an increased pressure load on the heart, myocytes will thicken as the heart must strengthen to push against a higher systemic pressure. Initially the heart is able to maintain function and this phase is considered adaptive hypertrophy. As pressure loading continues to increase and the walls continue to thicken, the response is no longer adaptive and the LV moves into maladaptive hypertrophy (*7*). In this case, the heart is unable to relax to drive the filling, and the much thickened walls create a very narrow flow path for blood entering the LV, resulting in abnormalities in the filling wave or, diastolic dysfunction. LV hypertrophy is diagnosed by an elevated left ventricular mass index which is the ratio of LV mass to body surface area (*10*-*12*).

In response to an increased volume load on the heart, myocytes typically lengthen in an attempt to increase the chamber size. This results in dilated cardiomyopathy as shown in the far right image of Figure 1.2. The dilated walls are unable to relax so the LV can fill properly, but the thin walls are also unable to contract to push blood out to the rest of the body. This condition results in both abnormalities in diastole and a decreased systolic function. Dilated cardiomyopathy is diagnosed by a sphericity index. The sphericity index is the ratio of the LV length to the LV width and the closer the value is to one the more dilated the LV (*13*).

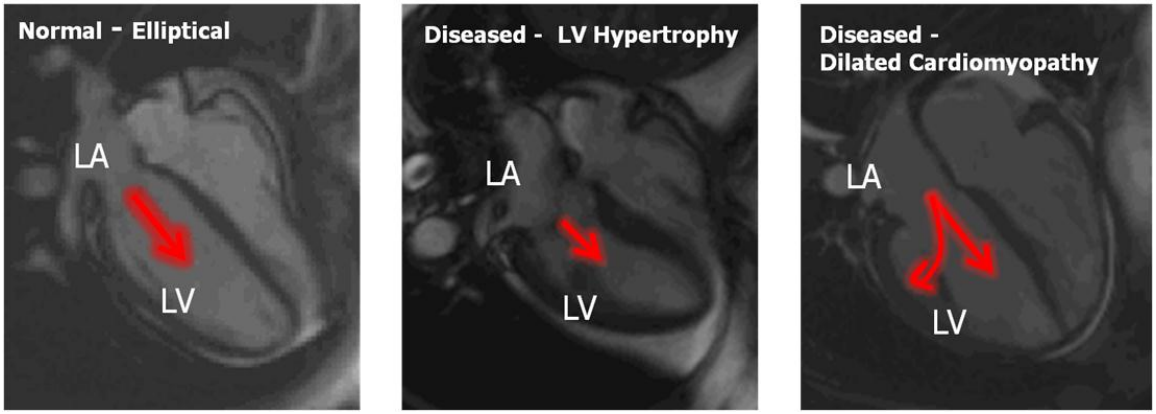

Figure 1.2: MRI Scans showing remodeled left ventricles in various states of disease. Left, normal LV. Center, hypertrophied LV showing thickened myocardial walls. Right, dilated LV showing thin walls and round, balloon shaped myocardium.

1.2.2 Left Ventricular Diastolic Dysfunction

After systole, the LV goes through a period of iso-volumic relaxation, prior to mitral valve opening, where the myocardium untwists, relaxes, and alters geometry to prepare for filling. The LV essentially acts as a suction pump (*14*), and when the LV pressure drops below the atrial pressure, the mitral valve is forced open and blood begins to enter the LV. This early diastolic filling wave creates an unsteady flow environment contained within a compliant vessel which is changing its geometry throughout the process. Complexities arise not only from a physiological standpoint, with many interrelated mechanisms affecting filling, but also from a fluid mechanics standpoint, making LV filling a difficult process to understand and therefore making LVDD difficult to diagnose.

LVDD is characterized by a decrease in LV relaxation, recoil, and myocardial compliance (*15*). The stiffer LV with impaired relaxation mechanisms is unable to sufficiently lower the internal pressure to drive the early filling wave. To account for this increased LV pressure, the left atrial pressure must increase (*16*). Being able to measure pressures in the LV and left atrium would be valuable to diagnosing LVDD. Pressures can be measured invasively using pressure catheters (*17*, *18*) or pulmonary capillary

wedge pressure, which is a measure of left atrial pressure (*19*) and is considered the best estimate for LV pressure. Both of these invasive pressure measurements are costly, time consuming, and present increased risks to patients, especially those with end stage heart failure (*20*). Due to the prevalence of LVDD and advancements in imaging technologies, it would be beneficial to utilize non-invasive techniques which are faster, more cost effective than and potentially just as useful as invasive measures.

1.2.3 Current Doppler based diagnostics

Clinically, there is no "gold standard" diagnostic parameter to recognize LVDD. Several parameters measured from Doppler echocardiography are used together to diagnose (*21*). An example of a mitral inflow Doppler is shown in Figure 1.3. This scan measures the velocity of blood crossing the center of the mitral valve in time. Several parameters are recorded and include peak E and peak A, which are the peak velocities crossing the mitral valve during early and late filling. The ratio of these two parameters, E/A, is useful as a diagnostic when used alongside other parameters (*21-23*). The deceleration time, is the time from peak early filling until the end of early filling and is plotted on Figure 1.3 as the time between the two vertical blue lines. The deceleration time has been shown to be closely related to the myocardial stiffness (*24, 25*).

Tissue Doppler, Figure 1.3center, is measured similarly to mitral inflow Doppler, only the transducer measures the velocity of either the lateral or the septal side of the mitral annulus. The mitral annulus moves upward, towards the atrium, during early filling, therefore the mitral annular velocity is recorded as a negative number, as it is moving away from the transducer. Increased mitral annular motion is a sign of a healthy LV as this indicates the walls are more compliant and able to move upward into the atrium to aid in the filling process. The ratio of E/E' has been shown to have improved diagnostic utility (*26, 27*) over just E or E' alone where E/E' less than 8 shows the LV is normal, E/E' greater than 15 shows the LV is diseased, and patients with E/E' in between 8 and 15 may require other parameters to give a final diagnosis (*26*).

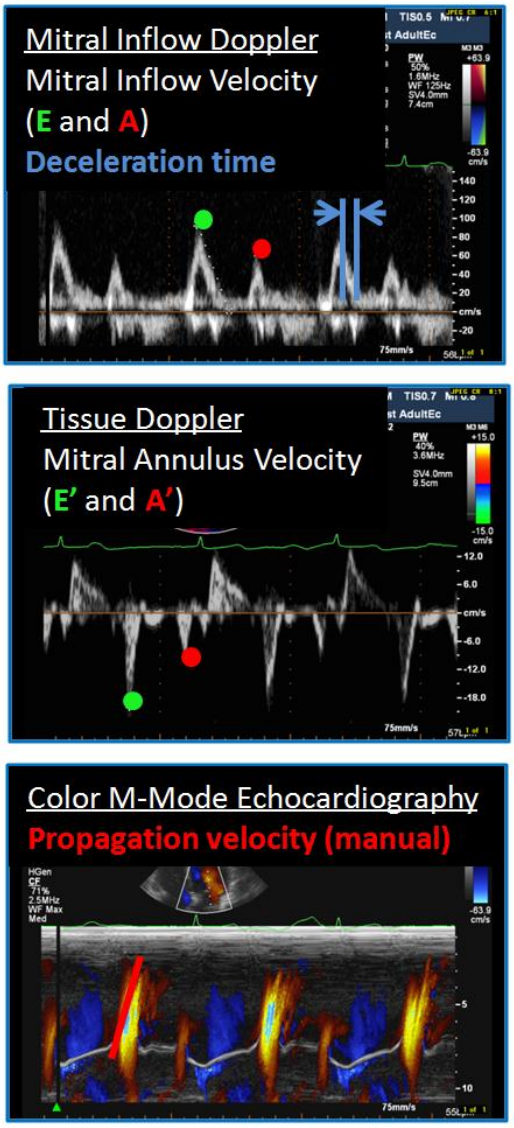

Figure 1.3: Conventional diagnostic parameters. Top shows a mitral inflow Doppler, measuring the velocity of blood crossing the mitral valve. Peak E velocity (green dot) and peak A velocity (red dot) are used to diagnose LVDD. The deceleration time, indicated by the two blue lines is related to LV relaxation. Middle shows tissue Doppler measuring the mitral annular velocity. E' and A' are indicated by the green and red dots. Bottom shows CMM echocardiography which records a line scan of centerline blood velocity from the mitral valve to the apex. These "waves" are used to evaluate filling or manually measure a propagation velocity (red line).

1.2.4 Color M-Mode Echocardiography: Velocity Analysis

Color M-Mode echocardiography, Figure 1.3 bottom and Figure 1.4, expands upon one dimensional Doppler scans by recording a line scan in time. The scan line is oriented along the length of the LV, centered in the mitral valve and extending to the apex, yielding a spatio-temporal map of velocity. These velocity maps of the filling wave allow for qualitative assessment of LV filling (*28, 29*).

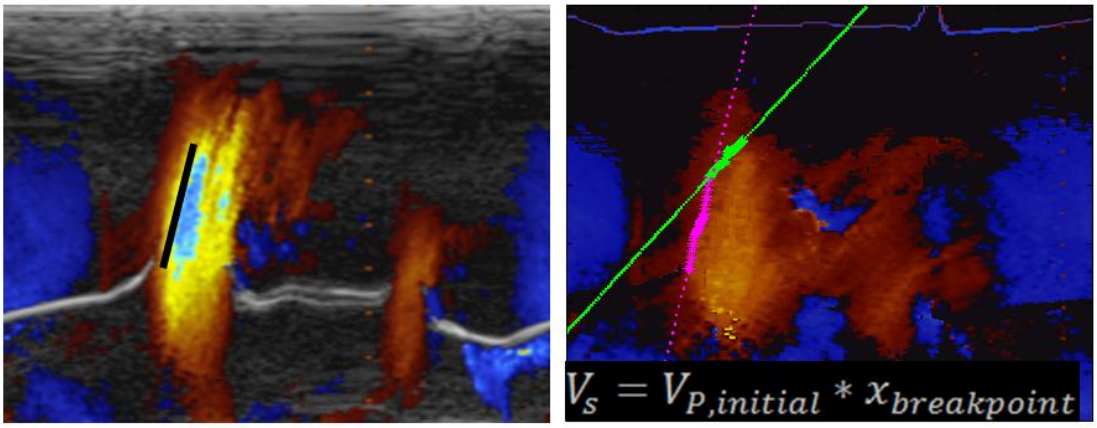

Figure 1.4: Left, conventional V_P measurement tracking the leading edge of the first aliasing boundary. Right, new V_S parameter, measuring an initial V_P and the distance the initial V_P extends into the LV, to calculate the new parameter

Many methods of quantifying a CMM wave propagation velocity, V_P, have been proposed (*28-32*). The current accepted method is to measure the slope of the leading edge of the first aliasing boundary from the mitral valve location to a distance 4cm into the length of the LV (*21*). The V_P is plotted in Figure 1.3 as the solid red line, and also in Figure 1.4 as the solid black line. The aliasing boundary is the yellow to blue transition and is typically set to around 50% of the maximum peak inflow velocity to optimize viewing of filling wave.

Previous work has shown that the V_P is highly dependent on the actual placement of the aliasing boundary (*28, 33, 34*). Others have noted that the leading edge is not necessarily linear (*35*) and may be better represented by two slopes (*36*). Previous work from our group developed a new parameter, V_S, or filling strength (*36*). This method uses an ensemble contour of a range of iso-velocities, instead of a single iso-velocity, removing some of the dependence on the aliasing boundary. The ensemble contour is used to identify an initial slope and a terminal slope, separated by a statistically significant breakpoint. The initial slope is plotted in pink in the bottom of Figure 1.4and the terminal slope is plotted in green. There is a clear point where the slope changes from a rapid initial slope to a much lower terminal slope. This point is called the break point. V_S is defined as the product of the initial slope and the distance that slope extends into the LV as defined in Equation 1-1.

$$V_s = V_{P,initial} * x_{breakpoint} \quad \textbf{1-1}$$

This parameter was found to have improved clinical utility over conventional V_P, which was manually measured and may also have more physical significance.

1.2.5 Color M-Mode Echocardiography: Pressure Analysis

CMM echocardiograms can also be used to non-invasively measure an intraventricular pressure difference (IVPD), (*14, 37-39*). The spatio-temporal velocity data can be used to solve the Euler equation (Equation 1-2) which is the inviscid, incompressible, one dimensional version of the Navier-Stokes equation (*3, 16, 18, 40*), as shown in Figure 1.5. This method has been validated against micromanometer pressure measurements, but still is subject to limitations that inhibit broader clinical utility.

$$\frac{\partial P}{\partial x} = -\rho\left[\frac{\partial U}{\partial t} + U\frac{\partial U}{\partial x}\right] \quad \textbf{1-2}$$

First it is important to note that this is a measure of the pressure difference along the length of the LV. It is measured relative to the mitral valve and therefore is not a measure of absolute pressure. This measure of "suction" would not account for an overall increase in LV and left atrial pressure, because it is relative (*14*, *37*). Previous concerns about the effect of scan line misalignment on the Doppler-derived IVPD value were addressed, and it was found that slight misalignment of the transducer scan line would have little effect on the resulting IVPD (*41*, *42*). In addition, concerns about the temporal resolution of the CMM echocardiograms being high enough to resolve accurate IVPD measurements have been raised (*43*). It was found using Taylor based error bounds, that the temporal resolution of the scan had a much greater chance for error based on low resolutions than the velocity resolution or the spatial resolution. Finally, slight variations between consecutive heartbeats due to noise or signal artifacts from the image acquisition process, may affect the resulting IVPD values. Very little has been done to address beat-to-beat variations, and it is typically assumed that the one beat chosen for analysis is representative of all heartbeats for that patient. Many of these limitations would have to be addressed before Doppler-derived IVPD has robust and reliable clinical utility.

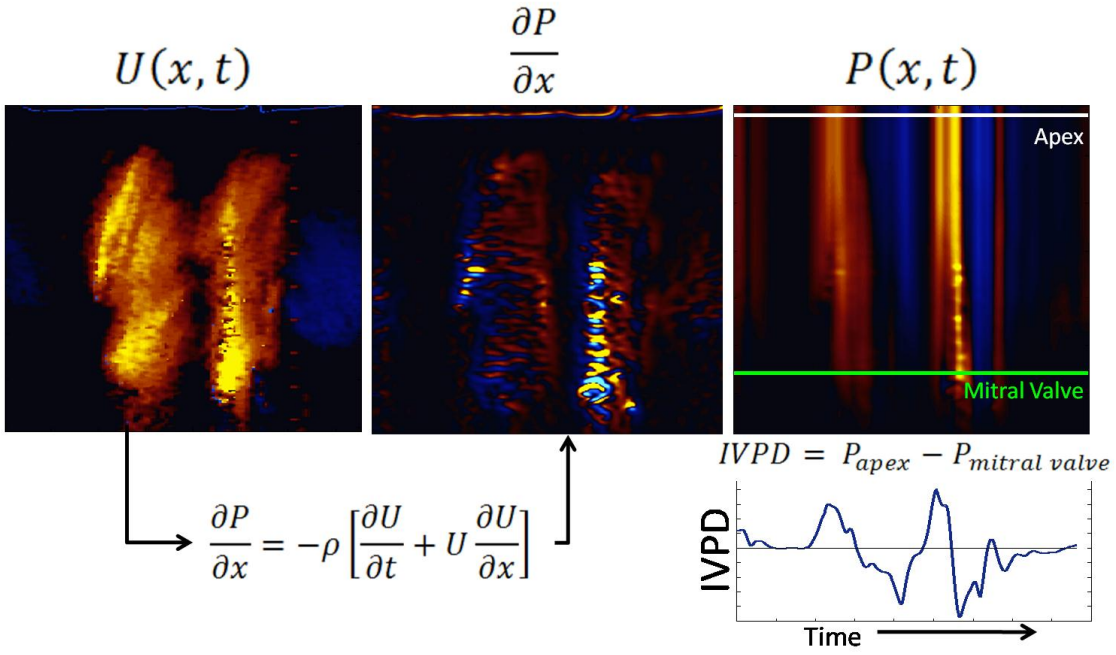

Figure 1.5: Solving the Euler equation to measure IVPD from Color M-Mode echocardiograms. Top, original velocity field U(x,t). Middle, resulting dP/dx field after using U(x,t) to solve the Euler equation. Next, P(x,t) after integrating dP/dx along the length of the LV. Bottom, IVPD referenced to the mitral valve location.

1.3 Structure of Thesis

This thesis consists of two manuscripts. First, I introduce a new methodology to perform a multi-beat spatio-temporal reconstruction on several CMM heartbeat recordings to reconstruct beats at a higher temporal resolution and also reconstruct a representative beat which takes into account beat-to-beat variations and eliminates variability from IVPD measurement. Second I address current limitations of measurement techniques for wave propagation velocity from a CMM echocardiogram and propose a new technique to better quantify these waves.

1.4 References

1. J. S. J. B. J. J. C. M. D. W. B. K. R. R. R. J. Redfield Mm, Burden of systolic and diastolic ventricular dysfunction in the community: Appreciating the scope of the heart failure epidemic. *JAMA: The Journal of the American Medical Association* **289**, 194 (2003).
2. T. E. Owan *et al.*, Trends in Prevalence and Outcome of Heart Failure with Preserved Ejection Fraction. *N. Engl. J. Med.* **355**, 251 (2006).
3. S. J. Khouri, G. T. Maly, D. D. Suh, T. E. Walsh, A practical approach to the echocardiographic evaluation of diastolic function. *Journal of the American Society of Echocardiography* **17**, 290 (2004).
4. P. M. Vandervoort, N. L. Greenberg, P. M. McCarthy, J. D. Thomas, in *Computers in Cardiology 1993, Proceedings.* (1993), pp. 293-296.
5. L. H. Opie, *The heart : physiology, from cell to circulation*. (Lippincott-Raven, Philadelphia, 1998).
6. R. A. O'Rourke. (McGraw-Hill Medical Pub. Division, New York, 2001).
7. L. H. Opie, P. J. Commerford, B. J. Gersh, M. A. Pfeffer, Controversies in ventricular remodelling. *Lancet* **367**, 356 (2006).
8. M. R. Zile, D. L. Brutsaert, New concepts in diastolic dysfunction and diastolic heart failure: Part II - Causal mechanisms and treatment. *Circulation* **105**, 1503 (Mar, 2002).

9. M. A. Konstam, D. G. Kramer, A. R. Patel, M. S. Maron, J. E. Udelson, Left ventricular remodeling in heart failure: current concepts in clinical significance and assessment. *JACC Cardiovasc Imaging* **4**, 98 (2011).
10. R. M. Lang *et al.*, Recommendations for Chamber Quantification: A Report from the American Society of Echocardiography's Guidelines and Standards Committee and the Chamber Quantification Writing Group, Developed in Conjunction with the European Association of Echocardiography, a Branch of the European Society of Cardiology. *Journal of the American Society of Echocardiography* **18**, 1440 (2005).
11. R. D. Mosteller, Simplified calculation of body-surface area. *The New England journal of medicine* **317**, 1098 (1987).
12. R. B. Devereux *et al.*, Echocardiographic assessment of left ventricular hypertrophy: Comparison to necropsy findings. *The American Journal of Cardiology* **57**, 450 (1986).
13. J. Madaric *et al.*, Early and late effects of cardiac resynchronization therapy on exercise-induced mitral regurgitation: relationship with left ventricular dyssynchrony, remodelling and cardiopulmonary performance. *Eur Heart J* **28**, 2134 (2007).
14. W. C. Little, Diastolic dysfunction beyond distensibility - Adverse effects of ventricular dilatation. *Circulation* **112**, 2888 (Nov, 2005).
15. J. D. Thomas, A. E. Weyman, ECHOCARDIOGRAPHIC DOPPLER EVALUATION OF LEFT-VENTRICULAR DIASTOLIC FUNCTION - PHYSICS AND PHYSIOLOGY. *Circulation* **84**, 977 (Sep, 1991).
16. T. E. Claessens, J. De Sutter, D. Vanhercke, P. Segers, P. R. Verdonck, New echocardiographic applications for assessing global left ventricular diastolic function. *Ultrasound Med. Biol.* **33**, 823 (Jun, 2007).
17. J. L. Dorosz, K. G. Lehmann, J. R. Stratton, Comparison of tissue Doppler and propagation velocity to invasive measures for measuring left ventricular filling pressures. *The American Journal of Cardiology* **95**, 1017 (2005).
18. A. Rovner *et al.*, Improvement in diastolic intraventricular pressure gradients in patients with HOCM after ethanol septal reduction. *American Journal of Physiology - Heart and Circulatory Physiology* **285**, H2492 (December 1, 2003, 2003).
19. H. P. Chaliki, D. G. Hurrell, R. A. Nishimura, R. A. Reinke, C. P. Appleton, Pulmonary venous pressure: Relationship to pulmonary artery, pulmonary wedge, and left atrial pressure in normal, lightly sedated dogs. *Catheterization and Cardiovascular Interventions* **56**, 432 (2002).
20. W. C. Little, J. K. Oh, Echocardiographic Evaluation of Diastolic Function Can Be Used to Guide Clinical Care. *Circulation* **120**, 802 (Sep, 2009).
21. S. F. Nagueh *et al.*, Recommendations for the Evaluation of Left Ventricular Diastolic Function by Echocardiography. *Eur. J. Echocardiogr.* **10**, 165 (March 1, 2009, 2009).
22. J. D. Thomas, Z. B. Popovic, Assessment of left ventricular function by cardiac ultrasound. *J. Am. Coll. Cardiol.* **48**, 2012 (Nov, 2006).

23. R. A. Nishimura, A. J. Tajik, Evaluation of diastolic filling of left ventricle in health and disease: Doppler echocardiography is the clinician's rosetta stone. *J. Am. Coll. Cardiol.* **30**, 8 (Jul, 1997).
24. W. C. Little, M. Ohno, D. W. Kitzman, J. D. Thomas, C.-P. Cheng, Determination of Left Ventricular Chamber Stiffness From the Time for Deceleration of Early Left Ventricular Filling. *Circulation* **92**, 1933 (October 1, 1995, 1995).
25. M. J. Garcia *et al.*, Estimation of left ventricular operating stiffness from Doppler early filling deceleration time in humans. *Am. J. Physiol.-Heart Circul. Physiol.* **280**, H554 (Feb, 2001).
26. S. R. Ommen *et al.*, Clinical utility of Doppler echocardiography and tissue Doppler imaging in the estimation of left ventricular filling pressures - A comparative simultaneous Doppler-Catheterization study. *Circulation* **102**, 1788 (Oct, 2000).
27. G. S. Hillis *et al.*, Noninvasive estimation of left ventricular filling pressure by e/e′ is a powerful predictor of survival after acute myocardial infarction. *J. Am. Coll. Cardiol.* **43**, 360 (2004).
28. P. Brun *et al.*, LEFT-VENTRICULAR FLOW PROPAGATION DURING EARLY FILLING IS RELATED TO WALL RELAXATION - A COLOR M-MODE DOPPLER ANALYSIS. *J. Am. Coll. Cardiol.* **20**, 420 (Aug, 1992).
29. M. J. Garcia, J. D. Thomas, A. L. Klein, New Doppler echocardiographic applications for the study of diastolic function. *J. Am. Coll. Cardiol.* **32**, 865 (Oct, 1998).
30. M. Stugaard, N. L. Greenberg, N. L. Klein, Does automatic quantification of color Doppler M-mode filling patterns differentiate constrictive from restrictive heart disease? *Circulation* **96**, 2628 (Oct, 1997).
31. R. Yotti *et al.*, Doppler-Derived Ejection Intraventricular Pressure Gradients Provide a Reliable Assessment of Left Ventricular Systolic Chamber Function. *Circulation* **112**, 1771 (September 20, 2005, 2005).
32. H. Takatsuji *et al.*, A new approach for evaluation of left ventricular diastolic function: Spatial and temporal analysis of left ventricular filling flow propagation by color M-mode doppler echocardiography. *J. Am. Coll. Cardiol.* **27**, 365 (1996).
33. M. Stugaard, C. Risoe, H. Ihlen, O. A. Smiseth, INTRACAVITARY FILLING PATTERN IN THE FAILING LEFT-VENTRICLE ASSESSED BY COLOR M-MODE DOPPLER-ECHOCARDIOGRAPHY. *J. Am. Coll. Cardiol.* **24**, 663 (Sep, 1994).
34. Y. Seo *et al.*, Assessment of propagation velocity by contrast echocardiography for standardization of color Doppler propagation velocity measurements. *Journal of the American Society of Echocardiography* **17**, 1266 (2004).
35. M. W. Sessoms, J. Lisauskas, S. J. Kovacs, The left ventricular color M-mode Doppler flow propagation velocity V-p: In vivo comparison of alternative methods including physiologic implications. *Journal of the American Society of Echocardiography* **15**, 339 (Apr, 2002).
36. K. C. Stewart *et al.*, Evaluation of LV Diastolic Function From Color M-Mode Echocardiography. *JACC: Cardiovascular Imaging* **4**, 37 (2011).

37. N. L. Greenberg, P. M. Vandervoort, M. S. Firstenberg, M. J. Garcia, J. D. Thomas, Estimation of diastolic intraventricular pressure gradients by Doppler M-mode echocardiography. *Am. J. Physiol.-Heart Circul. Physiol.* **280**, H2507 (Jun, 2001).
38. A. Rovner, N. L. Greenberg, J. D. Thomas, M. J. Garcia, Relationship of diastolic intraventricular pressure gradients and aerobic capacity in patients with diastolic heart failure. *Am. J. Physiol.-Heart Circul. Physiol.* **289**, H2081 (Nov, 2005).
39. J. D. Thomas, Z. B. Popovic, Intraventricular pressure differences - A new window into cardiac function. *Circulation* **112**, 1684 (Sep, 2005).
40. R. Yotti *et al.*, A noninvasive method for assessing impaired diastolic suction in patients with dilated cardiomyopathy. *Circulation* **112**, 2921 (Nov, 2005).
41. B. W. L. De Boeck *et al.*, Colour M-mode velocity propagation: a glance at intra-ventricular pressure gradients and early diastolic ventricular performance. *Eur. J. Heart Fail.* **7**, 19 (Jan, 2005).
42. N. L. Greenberg, S. Krucinski, P. M. Vandervoort, J. D. Thomas, Importance of scanline orientation for color Doppler M-mode diastolic inflow patterns and pressure gradient calculations. *J. Am. Coll. Cardiol.* **29**, 49166 (Feb, 1997).
43. J. L. Rojo-Álvarez *et al.*, Impact of image spatial, temporal, and velocity resolutions on cardiovascular indices derived from color-Doppler echocardiography. *Medical Image Analysis* **11**, 513 (2007).

2. Calculating CMM Intraventricular Pressure Difference using a Multi-Beat Spatiotemporal Reconstruction

Casandra Niebel[1] , Pavlos Vlachos[1], Min Pu[2], William Little[2]

[1]Department of Mechanical Engineering, Virginia Tech, Blacksburg VA

[2]Cardiology Section, Wake Forest Univ. Baptist Medical Center, Winston-Salem NC

2.1 Abstract

Objectives – This paper evaluates the effects of Color-M-mode (CMM) sweep speed and beat-to-beat variability on quantifying the left ventricular early diastolic intra-ventricular pressure difference (IVPD).

Background –IVPD is calculated by solving the Euler equation using CMM velocity data. At low sweep speeds, IVPD can be significantly underestimated. Moreover, scans may vary between heartbeats, meaning the IVPD of a single beat is not representative.

Methods – Proper Orthogonal Decomposition (POD) decomposes a CMM echocardiogram into a series of basis functions which contain a certain amount of the original signal energy. A CMM can be reconstructed by retaining any number of basis functions. By interpolating the basis functions and eliminating functions which do not contribute significantly to the signal energy, a higher resolution CMM, with less noise, can be reconstructed. Two normal subjects with at least 10 beats recorded at each sweep speed setting (25, 50, 75, 100, and 150 mmps) were used to analyze how scanner resolution affects IVPD and demonstrate the effectiveness of our method. Subsequently this procedure was applied to 3 normal cohorts (N1, n = 25; N2, n = 19; and N3, n = 9) and 2 diseased cohorts (R1, n = 17; and LVH, n = 17).

Results –For the two method demonstration subjects, the 25 mmps group resulted in a low median IVPD (1.68 mmHg and 1.90 mmHg), compared to the 150 mmps group, with

median IVPDs of (3.67 mmHg and 3.87 mmHg). Both patients' heartbeats, from all sweep speeds, were all reconstructed to 1.9 ms/pix and returned median IVPDs of 3.79 mmHg and 3.48 mmHg showing that there is a strong dependence of IVPD on the temporal resolution of the scan and that the reconstruction is capable of improving the quality of these low resolution CMM scan to return more accurate IVPDs. For the normal clinical cohorts the new method increased median IVPD from 3.1 mmHg to 3.49 mmHg for N1, 2.29 mmHg to 3.19 mmHg N2, and 1.77 mmHg to 3.09 mmHg N3, while the diseased cohorts increased from 2.28 mmHg to 2.89 mmHg for R1 and 1.45 mmHg to 2.27 mmHg for LVH, showing that the chance for a mis-diagnosis is much reduced after this new methodology is applied to CMM scans.

Conclusions – Beat-to-beat variations and temporal resolution affect the CMM derived IVPD. This can be overcome by a new method that rectifies CMM data recorded at low resolutions and allows for more accurate IVPD measurement independent of scanner acquisition settings.

2.2 Introduction

Color M-Mode echocardiography is conventionally used to qualitatively assess diastolic function, but recently a more quantitative analysis is gaining acceptance, especially for measuring intra ventricular pressure difference (IVPD) (*1-4*). Whereas a healthy ventricle functions as a suction pump and actively relaxes to drive the filling process, a diseased ventricle is unable to sufficiently lower its pressure to fill without an increase in left atrial pressure (*5*). Invasive measurements of IVPD require multiple catheter measurements and are not clinically feasible for diagnosis or follow up, due to high cost, time, and risk to the patient. In contrast, Doppler-derived IVPD could be a valuable non-invasive diagnostic alternative for LVDD although several limitations must be addressed before this method gains widespread clinical utility.

The temporal resolution of a CMM echocardiogram is limited by the sweep speed of the transducer which is directly related to the speed of sound in the blood or tissue, the sweep angle and the depth of scan. For a qualitative analysis, scanner resolutions are set

around 50 – 75 mm/s to record approximately 2 - 4 beats per screen shot. Moreover, each heartbeat recording may vary due to changes in transducer alignment or noise from the acquisition process. Therefore, it would be valuable to combine information from all available beats to generate a more quantitatively accurate representation of left heart filling.

We hypothesize that the temporal resolution and beat-to-beat variability affect the accuracy of Doppler-derived IVPD. In this work we present a novel methodology to enhance CMM data recorded at slower sweep speeds. In addition we present a method to account for beat-to-beat variability by reconstructing a single representative heartbeat from consecutive heartbeat scans. Combined, these tools provide a methodology for rectifying CMM data, improving accuracy of IVPD estimation and will potentially help reducing misclassifications of healthy or diseased subjects.

2.3 Methods

2.3.1 CMM Acquisition

Echo Doppler examinations were completed using either an iE33 (Philips Medical Systems, Andover, Massachusetts) or a Vivid E9 (General Electric Healthcare) ultrasound imaging system with a multiple frequency transducer. CMM echocardiograms were recorded in the apical long axis view with sweep speeds ranging from 25 to 150 mm/s and a color scale that optimized visualization as judged by the recording sonographer. In most research studies, the transducer sweep speed is kept constant across all patients. However, in a clinical setting the sweep speed may vary between patients, depending on laboratory echocardiography protocol and patient's heart rate. Images recorded on the GE machine were exported as a hierarchal data format (.HDF). The images from the Philips machines were exported as .PNG files.

2.3.2 Patient Cohorts

Two groups of CMM images are used in this analysis: (1) the proof of concept group and (2) the clinical validation group. The proof of concept group consists of 3

healthy subjects, each with at least 48 heartbeats recorded at 5 scanner sweep speeds of 25, 50, 75, 100, and 150 mm/s, with at least 9 beats per resolution group. This image group was recorded on a Philips machine and .PNG files were saved for analysis. The temporal resolution of each scan was determined from the time scale on the recorded images and the number of pixels between temporal scale tic marks. Details about the proof of concept group are listed in Table 2.1.

Table 2.1: Details about the scanner settings and temporal resolutions of the three proof of concept patients.

Proof of Concept Cohort						
	Patient 1 Depth of Scan = 18cm		Patient 2 Depth of Scan = 13 cm		Patient 3 Depth of scan = 18cm	
Scanner Sweep Speed (mmps)	Initial Temporal Resolution (ms/pix)	# of Beats	Initial Temporal Resolution (ms/pix)	# of Beats	Initial Temporal Resolution (ms/pix)	# of Beats
25	11.4	15	15.6	14	7.3	9
50	5.7	12	7.8	10	4.6	10
75	3.8	15	4.8	14	3.1	11
100	2.8	13	3.8	13	2.3	9
150	1.9	14	2.6	12	1.6	9

The clinical validation group consists of three normal filling sub-cohorts (N1, N2, and N3), one restrictive filling sub-cohort (R1) and one sub-cohort with severe left ventricular hypertrophy (LVH). The three normal sub-cohorts and the restrictive sub-cohort are classified based on peak early filling mitral inflow velocity, tissue Doppler mitral annular velocities and conventional propagation velocity, as recommended by the American Society of Echocardiography guidelines (*6*) and the severe LVH group is classified by an elevated left ventricular mass index (*7-9*). The details for each clinical validation sub-cohort are shown in Table 2.2.

Table 2.2: Clinical cohort characteristics for three independent normal filling sub-cohorts (light gray) and two independent diseased cohorts (dark gray)

Clinical Validation Cohort								
Cohort	File	# of patients	# of Beats	dt ms/pix	Age (yrs)	E/A	E/E'	Ejection Fraction
N1	.PNG	25	60	4.3	44.4 +/- 16.3	1.59 +/- 0.35	8.31 +/- 2.83	61.6 +/- 5.86
N2	.PNG	19	38	2.6	46.4 +/- 9.20	1.34 +/- 0.29	7.71 +/- 2.12	56.8 +/- 0.44
N3	.HDF	9	24	9.4	46.4 +/- 16.2	na	na	56.7 +/- 5.24
R1	.PNG	17	45	4.3	61.9 +/- 13.3	2.90 +/- 1.05	17.8 +/- 7.90	28.6 +/1 8.13
LVH	.HDF	17	35	9.4	57.5 +/- 11.3	na	na	27.1 +/- 14.0

Values reported are mean +/- one standard deviation. E/A is the ratio of the peak mitral inflow velocities recorded using mitral inflow Doppler and E/E' is the ratio of peak early mitral inflow velocity to peak early tissue velocity.

Patients were all undergoing clinically indicated echocardiography at the Wake Forest University Baptist Medical Center. The study was conducted according to protocols approved by the Virginia Tech and Wake Forest University Baptist Medical Center institutional review boards.

2.3.3 Doppler derived IVPD

The Doppler derived IVPD is noninvasively calculated using the spatio-temporal velocity data from a CMM echocardiogram to solve the Euler equation (*1*). The Euler equation, Equation 2-1, is the one dimensional Navier-Stokes equation assuming incompressible and inviscid flow, where U is velocity, P is pressure and ρ is the density of blood.

$$\frac{\partial P}{\partial x} = -\rho\left[\frac{\partial U}{\partial t} + U\frac{\partial U}{\partial x}\right] \qquad \text{2-1}$$

The spatial and temporal derivative of the velocity field are calculated and used to calculate $\frac{\partial P}{\partial x}$ as shown in Figure 2.1. The line integral along the length of the ventricle is calculated at each time step, yielding a temporal profile of pressure values $P(x,t)$. A temporal profile of IVPD is calculated by subtracting the pressure at the mitral valve from the pressure at the apex. The peak IVPD during early filling is then identified. This method has been validated with comparisons to direct invasive pressure measurements by micro manometers (*1-3, 10*).

The echocardiograms were analyzed using an in-house algorithm developed in MATLAB (The Mathworks, Natick, MA), which first performs a velocity reconstruction and then a dealiasing algorithm before evaluating the Euler equation and estimating the IVPD (*11*).

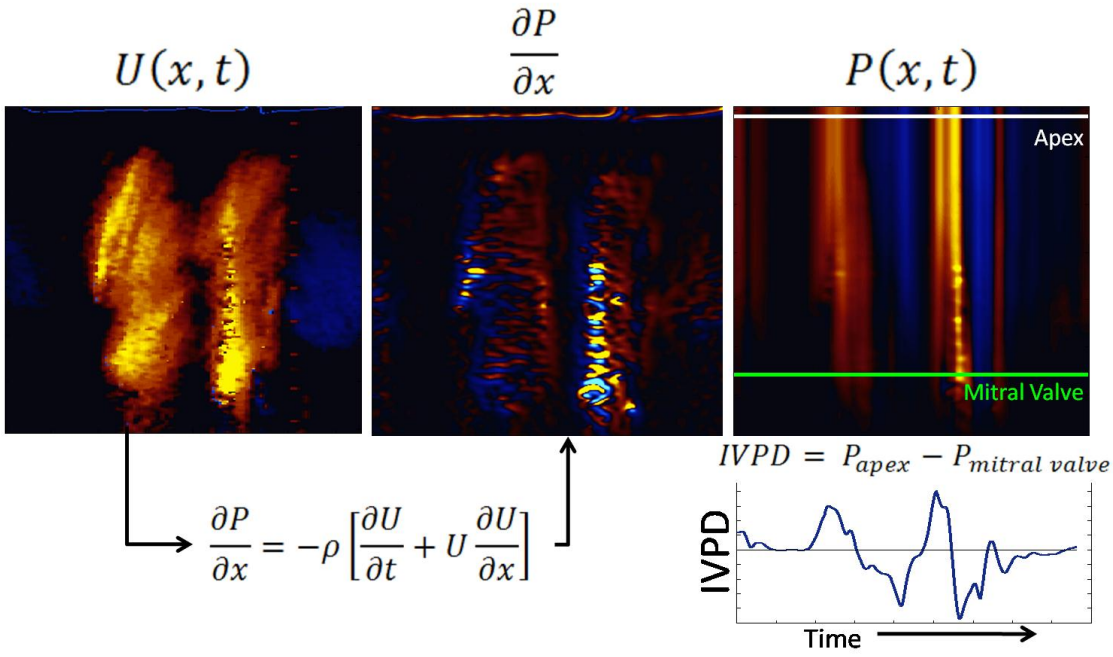

Figure 2.1: Doppler-derived IVPD calculation. The velocity field U(x,t) is used to solve the Euler equation and generate a map of the pressure gradient dP/dx. This pressure gradient is integrated to solve for the pressure, P(x,t). The IVPD is calculated by measuring the pressure at the apex relative to the pressure at the mitral valve location. The peak value during early diastole is recorded as the peak IVPD in mmHg.

2.3.4 Proper Orthogonal Decomposition Reconstruction Methodology

The new methodology presented here achieves two objectives:

1. First, to increase the temporal resolution of CMM echocardiograms recorded at low sweep speeds without increasing noise and
2. Second, to reduce beat-to-beat variability by combining velocity information from a series of heartbeats in order to reconstruct a single heartbeat.

Both of these objectives are accomplished through the development of a novel method based on proper orthogonal decomposition (POD), which allows us to combine information from multiple beats, perform a spatiotemporal reconstruction of the CMM data increasing temporal resolution and signal-to-noise ratio while reducing artifacts and produce a representative heartbeat.

2.3.5 Proper Orthogonal Decomposition

Proper orthogonal decomposition (POD) is a method commonly used in signal processing to decompose spatio-temporal data to a finite number of orthogonal basis functions (modes) that are optimized to capture the maximum energy contained in the signal (*12-14*). The most energetic modes represent the dominant features in the signal and the lower energy modes are more likely to represent random noise or other signal artifacts. Similar to how a Fourier analysis represents any signal as a series of sine and cosine waves at varying frequencies and with respective magnitude coefficients; the POD represents any signal as a series of energetically optimal mode shapes, φ_i, and corresponding temporal coefficients, a_i as shown in Equation 2-2.

$$U(x,t) = \sum_{i=1}^{N} a_i(t)\varphi_i(x) \qquad \textbf{2-2}$$

Here POD is applied to a series of CMM heartbeats which are represented as a matrix of velocity values $U(x,t)$ as shown in Figure 2.2. All available beats are aligned sequentially, with distance plotted on the y-axis and time on the x-axis. POD

decomposes the original velocity matrix (size m x n), into a series of mode coefficients (a_i, size m x n), and mode shapes (φ_i, size n x n). As shown in Figure 2.2, the initial mode coefficients have a higher magnitude and a clear structure, where the last mode coefficient, N, is low magnitude noise. Likewise, the initial mode shapes capture dominant features in the signal whereas the final modes are noisy with no clear structure.

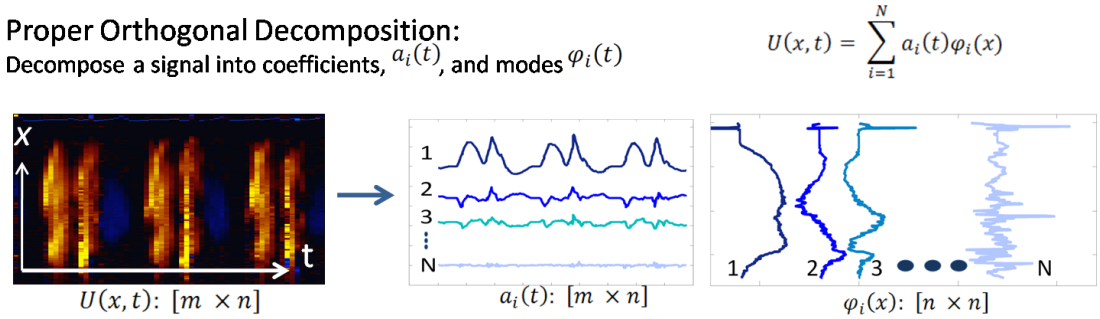

Figure 2.2: Proper Orthogonal Decomposition (POD) applied to a series of heartbeats. The raw image is decomposed into a series of mode coefficients $a_i(t)$, and mode shapes $\varphi_i(x)$. Each mode contains a certain amount of energy from the original signal, with initial modes (1, 2, and 3 above) containing the most energy and representing dominant features in the signal and the final modes (N above) representing noise and signal artifacts. The matrix of mode coefficients is sized [m x n] and the matrix of mode shapes is sized [n x n]. Reconstructing the signal using all modes will return the original signal. A signal with reduced noise can be reconstructed by discarding some non-significant modes.

2.3.6 Selection of a Cutoff Mode

Once POD is performed the next step is to select the appropriate number of modes that should be retained in the reconstructed signal. If all modes are included, the original signal would be recovered with all of the noise and artifacts. Therefore the proper reconstruction should retain only modes that contain useful signal information and discard modes containing noise and artifacts. The number of POD modes that optimally reconstruct a signal is a critical question in POD. In order to avoid heuristics and user dependent inputs an approach for objective determination of the cutoff mode is needed.

Using POD mode entropy is one possible approach (*15*). Here the entropy represents the amount of information in the signal. First, all modes are sorted by the amount of energy that each mode contains and the cumulative mode energy as a function of mode number is calculated. This energy spectrum is then utilized to choose a cutoff mode, where a reconstruction with all modes prior will contain a certain fraction of the total energy in the original signal.

Each mode contains a certain amount of energy, λ_k, from the original signal and the normalized energy contained in each mode is defined in Equation 2-3. The POD mode entropy, H_k, is defined in Equation 2-4 (*15*).

$$E_k = \frac{\lambda_k}{\sum \lambda_k} \quad \textbf{2-3}$$

$$H_k = -\frac{1}{\log(K)} \sum_{k=1}^{K} p_k log(p_k) \quad \textbf{2-4}$$

An example POD mode entropy spectrum is plotted in Figure 2.3. The POD mode entropy increases with each mode and eventually plateaus. A plateau in the entropy spectrum indicates that all significant information is contained in the modes prior to that point. Any additional modes are not contributing significant information and are most likely contributing to noise in the signal. A change point analysis is then used to objectively identify this plateau point (*16, 17*). A change point analysis locates the most statistically significant change in a data series.

$$cumulative\_sum_k = cumulative\_sum_{k-1} + (H_k - \overline{\overline{H}}) \quad \textbf{2-5}$$

This plateau point is the cutoff mode, C, and is indicated by the red point on the entropy spectrum in Figure 2.3. All modes prior to mode C are retained and used in the reconstruction and any subsequent modes are discarded.

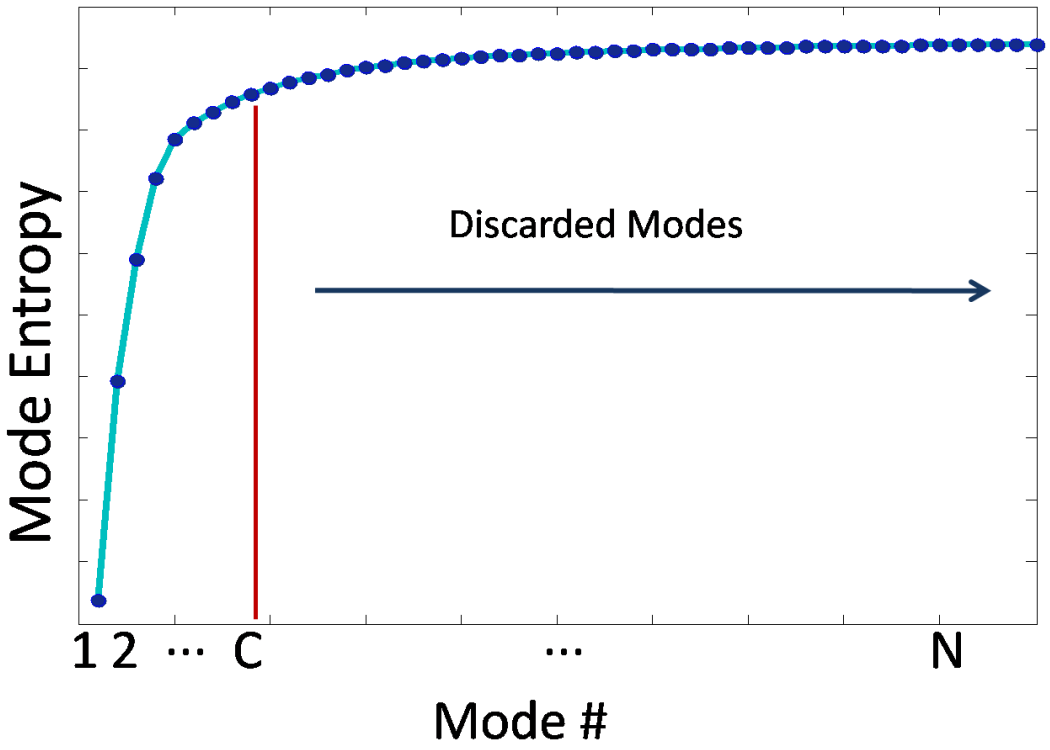

Figure 2.3: Selection of a cutoff mode determines the level of noise that will remain in the reconstructed signal. The normalized mode energy is the normalized amount of energy contained in each mode. The mode entropy is then calculated from the normalized mode energy. As the mode entropy reaches a maximum value, this indicates that all significant information is contained in the prior modes. To locate this "plateau" where the entropy spectrum levels off, a change point analysis is used to locate the most statistically significant change in the entropy spectrum. This mode is chosen as the cutoff mode. All modes prior are retained; all following modes are discarded.

2.2.7 Interpolate Mode Temporal Coefficients

Next, the temporal coefficients for each retained POD mode are re-sampled to the desired resolution using a spline function. At this point, there is the option to reconstruct each beat individually, or to synthesize the mode coefficient information across all beats in order to reconstruct one representative beat. Both of these options are pictured in

Figure 2.4. To reconstruct individual beats, all mode coefficients are interpolated to the desired resolution. To reconstruct one representative beat, the median of the mode coefficients across all beats is calculated and this median signal is interpolated.

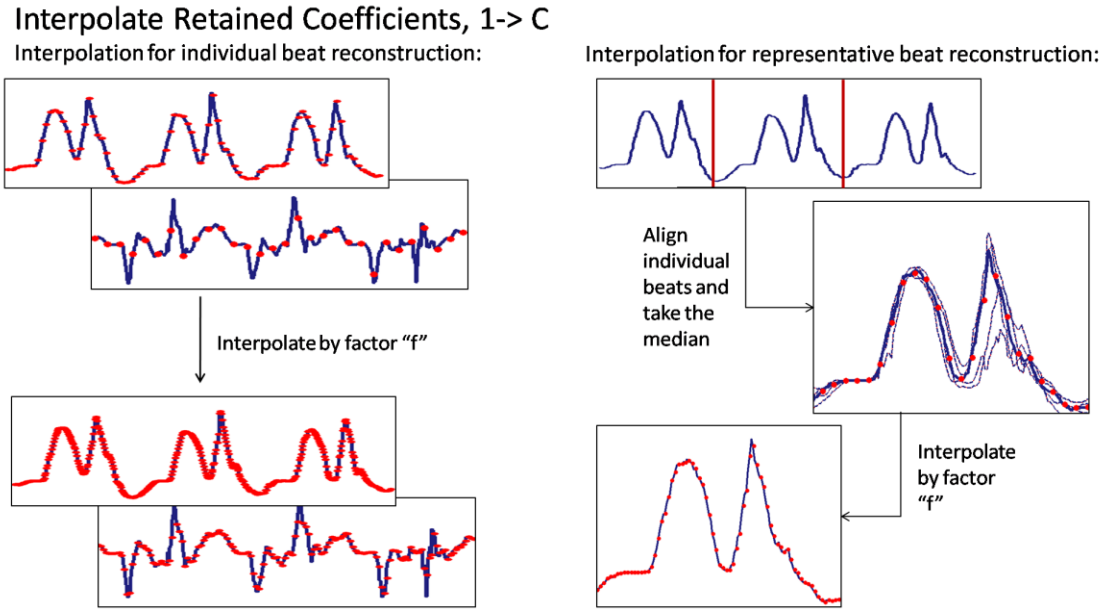

Figure 2.4: The retained temporal mode coefficients are interpolated to improve the resolution of the reconstructed signal. To interpolate for the individual beat reconstruction, the all retained mode coefficients (1→ C) are interpolated to the desired resolution. This new matrix of temporal mode coefficients is now [mf x c]. To interpolate for the representative beat reconstruction, the median value the temporal coefficients for all beats is calculated for all temporal mode coefficients. This median is then interpolated to the desired resolution.

2.3.8 Signal Reconstruction

The final CMM is reconstructed using the interpolated mode coefficients and retained modes. A comparison between the original signal, the individual reconstructed beats, and the representative beat are shown in Figure 2.5. The original signal has a lot of noise and a low temporal resolution. The individual reconstructed beats have significantly improved temporal resolution. The reconstructed beat contains similar

features to those seen in the individual reconstructed beats and has removed any effects from beat-to-beat variability.

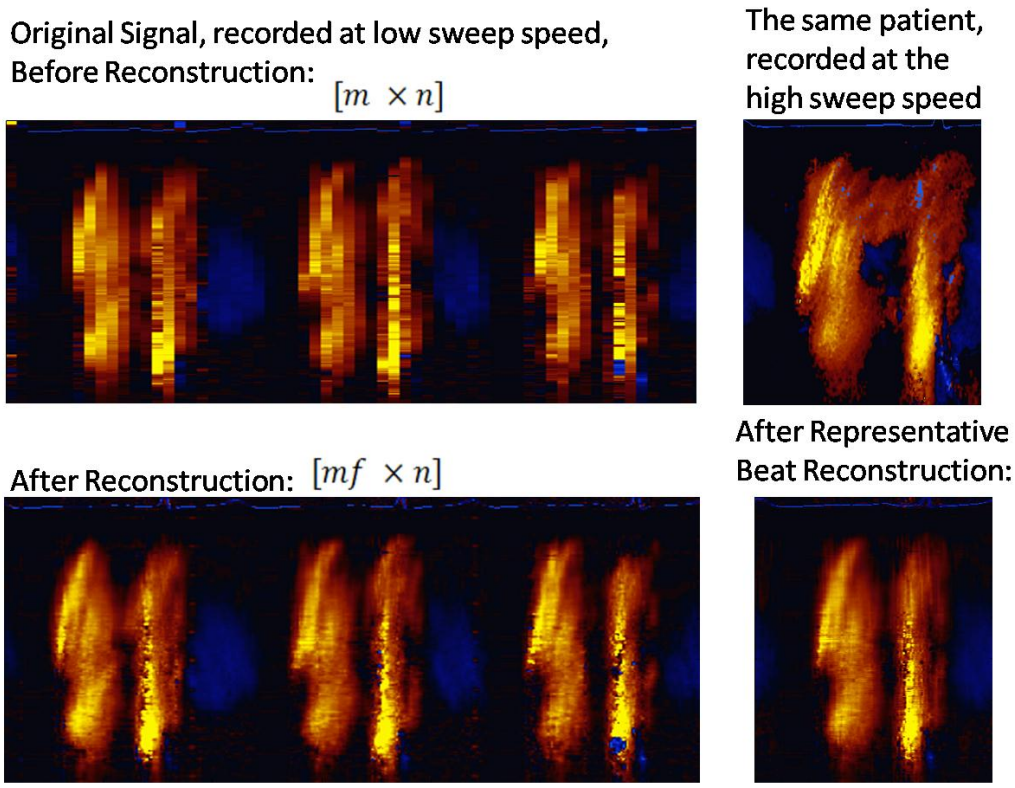

Figure 2.5: Signal Reconstruction. Prior to reconstruction, the signal is an [m x n] matrix with low resolution and a noisy signal. After reconstructing the individual beats using the retained interpolated mode coefficients, the signal is now and [mf x n] matrix with improved resolution. The representative beat reconstruction is also shown and clearly has similarities to all three beats, but has accounted for small beat-to-beat changes. An original signal recorded at the highest scanner sweep speed is also included for comparison.

These two outputs achieve the objectives of this method. First, the individual beat reconstructions increase the temporal resolution of CMM echocardiograms recorded at low sweep speeds, allowing for Doppler-derived IVPD to be calculated accurately and for comparison between patients recorded at different sweep speeds. Second, the representative beat, retains only the common information present across all heartbeats

and reconstructs one heart cycle that accounts for beat to beat variation, providing one beat which is representative of the filling pattern for that specific patient.

2.4 Results

2.4.1 Proof of Concept Group

For the proof of concept group the IVPD was calculated for all beats at all sweep speeds prior to POD interpolation and after doing a POD reconstruction to 1.9 ms/pixel. In Figure 2.6, each row of plots is one normal subject. The left column shows the IVPD value for each beat before reconstruction, as a function of scanner sweep speed. It is evident that the IVPD estimation is greatly dependent on the scan resolution. The lowest sweep speeds show a median IVPD of 1.68 mmHg, 1.90 mmHg, and 3.15 mmHg respectively, two of which would be suggestive of disease. The highest sweep speeds have a median IVPD value of 3.67 mmHg, 3.87 mmHg and 5.15 mmHg, which are values consistent with normal subjects. The right column plots show the IVPD of each beat after POD reconstruction to a uniform resolution, which resulted in IVPD values very similar across all scanner sweep speed groups. The red dots indicate the IVPD value from the representative beat, which is similar to the median value for each group as expected. These results provide evidence that the methodology presented here rectifies the CMM data in such a way that the IVPD estimation is independent of the natively recorded sampling rate.

There is also an increase in scatter in the lower resolution groups as the beats are reconstructed to higher resolutions. The scatter in the reconstructed IVPD values is similar to the scatter observed in the highest resolution original IVPD values. This suggests that there may be a limit as to how high of a resolution these beats can be reconstructed to. At some point, the analysis will begin incorporating more noise into the image than was there previously. For this reason, higher resolutions were investigated.

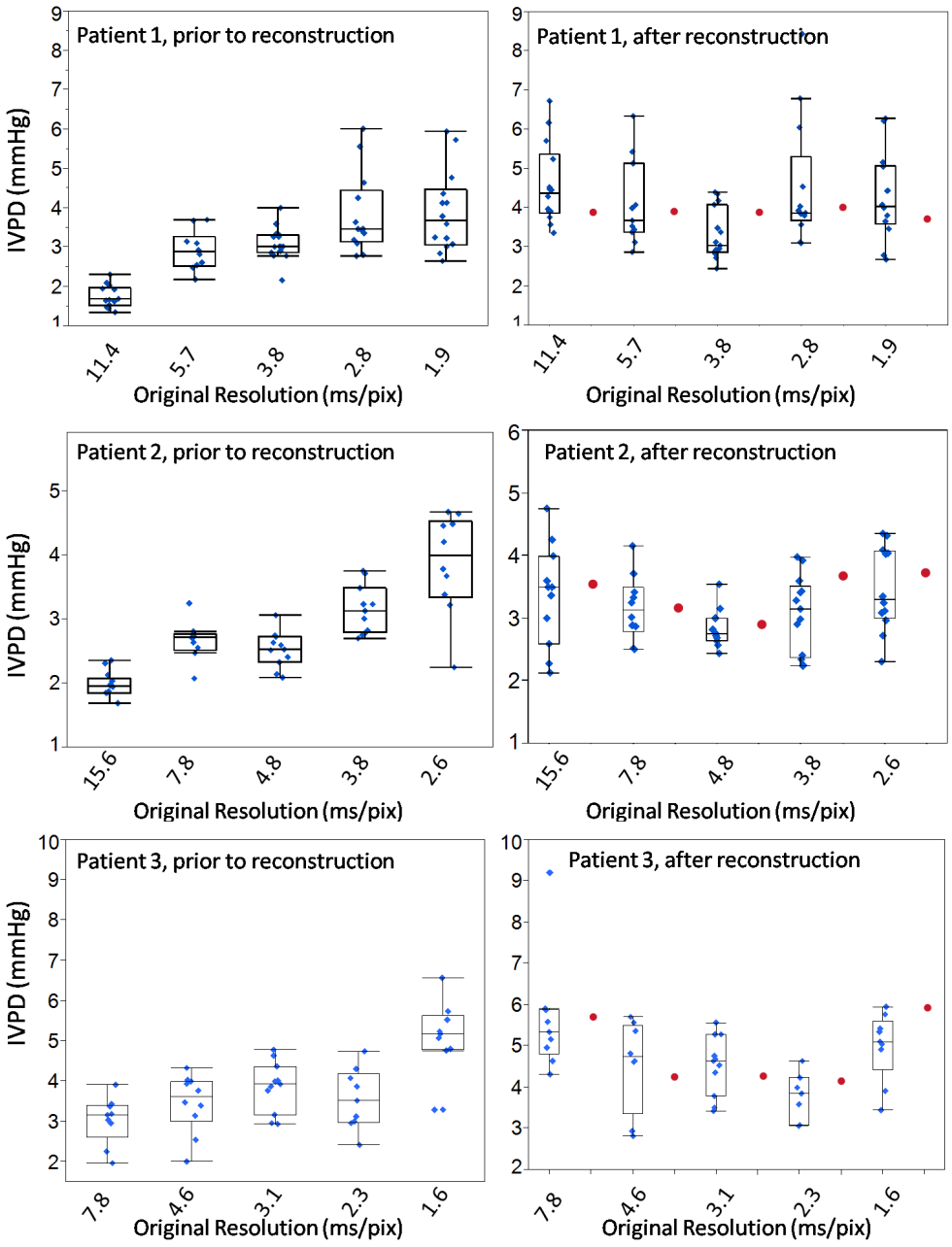

Figure 2.6: The top row shows the results for the first normal subject from the proof of concept cohort. The plot on the left shows the Doppler derived IVPD value from each beat for each original resolution group. All groups are reconstructed to the highest observed scanner resolution (1.9 ms/pix) and these results the IVPD from the reconstructed scans is plotted on the left. Reconstructed beats are representative of all beats for each original resolution group and are plotted as the single red circles. The second and third rows show the same trends.

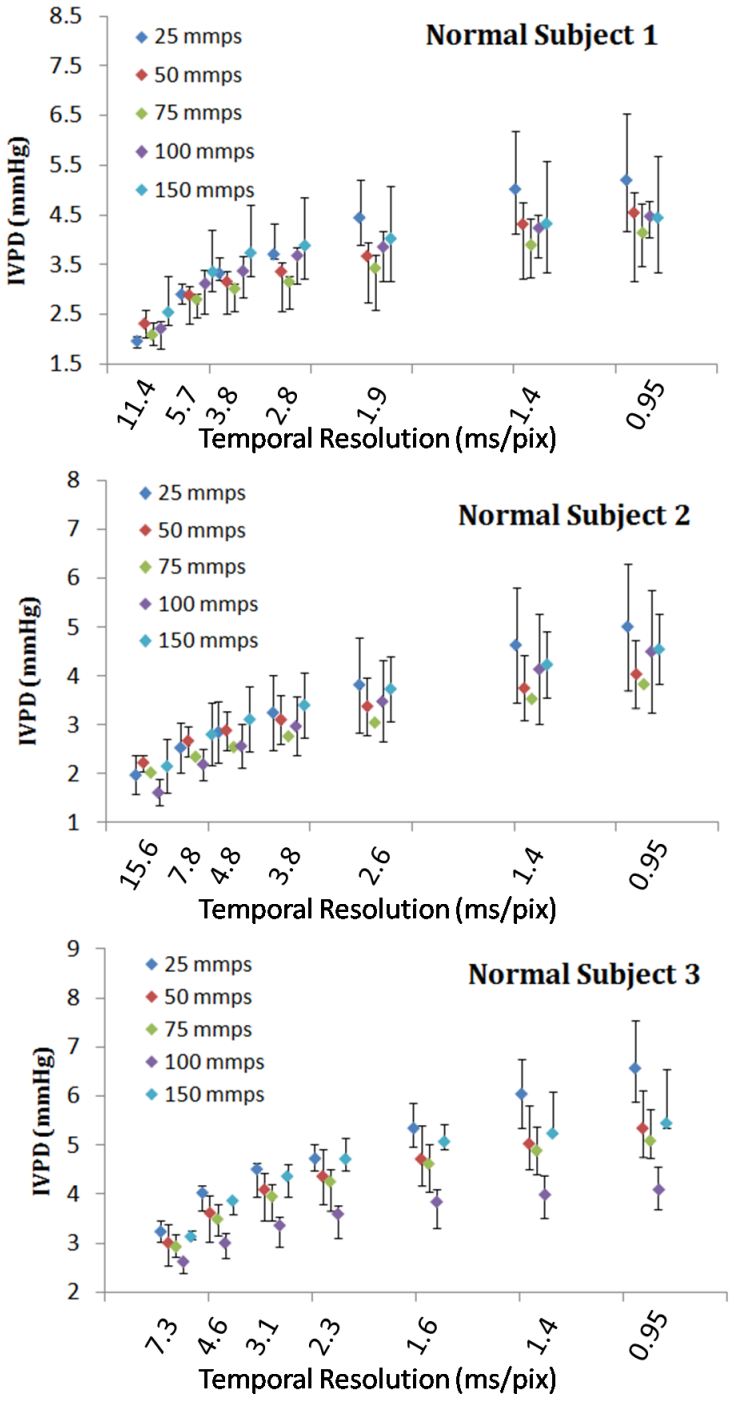

Figure 2.7: All original resolution groups reconstructed at all possible temporal resolutions using POD mode interpolation. All data points are slightly offset for viewing.

The data was re-sampled to all observed scanner resolutions and to two resolution values (1.4 ms/pix and 0.95 ms/pix) higher than the highest scanner resolution. Figure 2.7shows the plots of median IVPD versus up or down sampled resolution for all scanner sweep-speed groups. The bars represent the 25% and 75% quartiles.

This analysis was used to determine if further increasing the scan resolution would increase scatter in the data and if the IVPD value would plateau (converge to a certain value), which would illustrate that above a certain reconstruction sampling-rate the results become independent of the scan sweep-speed. Figure 2.7 shows that above a rate of 1.9 ms/pix the IVPD value is not affected but the inter quartile range does increase with increased temporal resolution. Thus, interpolating to highest resolutions appears to increase the random error in the IVPD estimation. Therefore, for the present analysis 1.9 ms/pix was chosen to reconstruct the clinical cohort.

2.4.2 Clinical Group

The POD mode interpolation method was used to reconstruct all clinical sub-cohorts' beats at 1.9 ms/pix. All of these patients had either two or three beats recorded which were used to generate a representative beat for each patient. The POD mode interpolation increased the group median for all five clinical cohorts with group median values reported in Table 2.3. The cells with multiple entries show the median of all individual beat values (all beat 1, all beat 2, all beat 3) and the cells with single entries show a median value of all beats (1, 2 and 3 combined) with the exclusion of the representative beat row, which shows the median of all representative beats for that sub-cohort. In all three normal sub-cohorts, the group median IVPD increased to a normal range (3.10 mmHg to 3.49 mmHg for N1, 2.29 mmHg to 3.41 mmHg for N2, and 1.77 mmHg to 3.09 mmHg for N3).

Prior to reconstruction, groups N2 and N3 would have been classified as diseased. The two diseased sub-cohorts also showed a slight increase in group median IVPD, but both groups still remain within the range for diseased filling, (2.28 mmHg to 2.89 mmHg for R1 and 1.45 mmHg to 2.27 mmHg for LVH). These results show that although the reconstruction is increasing the median IVPD for all sub-cohorts, the diseased cohorts

still maintain low IVPD values, while the normal cohorts increase median IVPD into a healthier range of IVPDs, implying that this methodology may reduce mis-diagnosis. For all patient groups, the reconstructed beat IVPD is comparable to the group median. This shows that the representative beat is providing a good representation of the filling by incorporating information from a series of beats, reducing erroneous IVPD measurements as a result of an artifact that may only appear in one beat.

While the IVPD values are now in the appropriate ranges, it is still unclear whether the new methodology improves the clinical utility of IVPD. Receiver operator characteristic curves and the resulting AUC were calculated for each normal and diseased sub-cohort combination (LVH with N1, N2, N3 and R1 with N1, N2, N3). The AUCs for all sub-cohort groupings for six parameters are in Table 2.4. The six variables used in this analysis were original IVPD for two beats, individual reconstructed IVPD for two beats, the mean of all individual reconstructed IVPDs, and the representative beat IVPD. The LVH group had a very low original temporal resolution (and low original IVPD), therefore, when the LVH group is compared with the two higher resolution normal filling cohorts (N1 and N2), all parameters have a high AUC (all > 0.89). The diagnostic capability is good for all parameters because of the inherent flaw in how the data was recorded. All diseased patients were recorded at a low resolution and all normal patients were recorded at a high resolution. When the LVH group is compared with N3 (also low resolution scans initially), there is an improvement in AUC from the original analysis (AUC = 0.786 and 0.694) to the individual interpolated beat analysis (AUC = 0.889 and 0.883), to the representative beat analysis (AUC = 0.917).

The R1 cohort was recorded at a higher resolution. In all three of these ROC curves (with N1, N2, and N3), we observe an improvement in AUC for both the mean of all individual reconstructed IVPDs and the representative beat IVPDs. In the comparison of R1 (initially high resolution) and N3 (initially low resolution), the original beat IVPDs report an AUC of less than 0.50. This means that these two groups show the reversed trend from what is expected. The diseased group has higher IVPD than the normal cohort. Simply due to the temporal resolutions of these scans, this normal filling cohort would be diagnosed as diseased and this diseased cohort would be considered normal.

A Tukey-Kramer HSD test was also performed to compare the means of each normal sub-cohort with each diseased sub-cohort, prior to reconstruction (two individual beats), after the individual beat reconstruction (two individual beats), using the mean of all individual beat IVPDs, and after the representative beat reconstruction using a significance value of 0.05. The results from the Tukey-Kramer analysis are presented in Table 2.4. The individual original beats correctly identify significant differences between 4 and 2 out of 6 groupings. The individual reconstructed beats correctly identify differences between 4 and 4 out of 6 groupings and the mean of the reconstructed beats and the representative beat correctly identify 5 and 5 out of 6 differences. These results show an improved ability to differentiate between normal and diseased filling after the reconstruction. The Tukey-Kramer test was also applied to see if all normal cohorts would be grouped together (means not significantly different) before and after the reconstruction. We see a slight improvement in the similarity between means from the original analysis (1 and 1 out of 3 correct) to the reconstructed analysis (1 or 2 out of 3 correct).

Two larger groupings of patients from the clinical cohort were chosen to test diagnostic capability using ROC curves in larger cohorts. The groups were selected to attempt to keep the number of normal and diseased patients approximately equal in each grouping. The binary variable was the known clinical classification (normal, 0; diseased, 1) and the continuous variable was varied to include all parameters from the sub-cohort combination analysis (original IVPD value from two beats, the individual reconstructed IVPD from two beats, the mean of the individual reconstructed IVPDs and the representative beat IVPD). The two groupings chosen were LVH and R1 (n = 34) and N1 and N3 (n = 34) for the first and LVH and R21 (n = 34) and N2 and N3 (n = 28) for the second. These ROC curves are plotted in Figure 2.8. These plots show an increase in area under the curve (AUC) for all of the reconstructed beats, when compared with the original beat IVPDs. This shows that the new methodology improves the diagnostic capability of IVPD.

Table 2.3: Clinical Cohort Results – Original individual beat IVPDs, Original median IVPDs, Reconstructed individual beat IVPDs, Reconstructed median IVPDs, and Representative beat IVPDs for all clinical group sub-cohorts

Clinical Validation Cohort Results										
	N1		N2		N3		R1		LVH	
	Med	IQR	Med	IQR	Med	IQR	Med	IQR	Med	IQR
Single Beat IVPD	2.93 2.70 3.34	1.42 0.99 0.91	2.45 2.27	1.05 1.45	1.77 1.81 1.63	0.25 0.12 1.07	2.28 2.34 2.18	0.67 1.05 0.69	1.46 1.45 1.38	0.43 0.90 0.58
Median IVPD, all single beats	3.1	1.33	2.29	1.13	1.77	0.45	2.28	0.82	1.45	0.71
Individual Reconstructed Beat IVPD	3.38 3.51 3.60	1.01 1.07 1.08	3.28 3.64	1.60 1.66	3.07 3.12 3.02	1.51 1.04 1.22	2.63 3.02 2.93	0.98 1.31 1.03	2.55 2.32 1.99	1.44 2.21 0.56
Median IVPD, all individual reconstructed beats	3.49	1.01	3.41	1.57	3.09	1.44	2.89	1.27	2.27	1.72
Representative Beat IVPD	3.39	0.91	3.19	0.98	2.98	1.28	2.80	0.93	2.02	1.11
Values reported are median IVPD in mmHg and inter quartile range (75% - 25%)										

Table 2.4: Top table reports the area under the curve of a receiver operator characteristic comparing all normal and diseased combinations. Bottom table, resulting p-values from a Tukey-Kramer HSD test comparing all groups that should be statistically different (ie, normal and diseased) and all normal sub-cohorts which should be statistically the same. The grey cells indicate the correct result from the means comparison. The mean of the individual reconstructed beats and the representative beat perform the best and come to the correct conclusion 6 out of 9 and 7 out of 9 times respectively.

Area Under the Curve from Receiver Operator Characteristic						
	Original 1	**Original 2**	**Reconstructed 1**	**Reconstructed 2**	**Reconstructed Mean**	**Representative Beat**
LVH , N1	0.967	0.929	0.92	0.894	0.958	0.993
LVH, N2	0.876	0.846	0.771	0.755	0.810	0.869
LVH, N3	0.786	0.694	0.889	0.883	0.900	0.917
R1, N1	0.7422	0.6711	0.738	0.796	0.811	0.7844
R1, N2	0.509	0.534	0.522	0.549	0.566	0.627
R1, N3	0.439	0.327	0.772	0.806	0.850	0.689
P-values from Tukey-Kramer HSD test						
	Original 1	**Original 2**	**Reconstructed 1**	**Reconstructed 2**	**Reconstructed Mean**	**Representative Beat**
LVH , N1	<0.0001*	<0.0001*	<0.0001*	<0.0001*	<0.0001*	<0.0001*
LVH, N2	0.0018*	0.0012*	0.2014	0.1993	0.0451*	0.0048*
LVH, N3	0.1889*	0.5488	0.005*	<0.0001*	<0.0001*	<0.0001*
R1, N1	0.0311*	0.2821	0.0095*	0.0035*	0.0008*	0.0013*
R1, N2	0.9663	0.9276	0.9979	0.6776	0.8806	0.8677
R1, N3	0.979	0.7391	0.0474*	<0.0001*	0.0004*	0.0175*
N1, N2	0.0166*	0.0451*	0.0098*	0.0180*	0.0039*	0.0029*
N2, N3	0.9658	0.4756	0.0907	0.0250*	0.0064*	0.1387
N1, N3	0.0112*	0.0220*	1.0000	0.9750	0.9622	0.9714

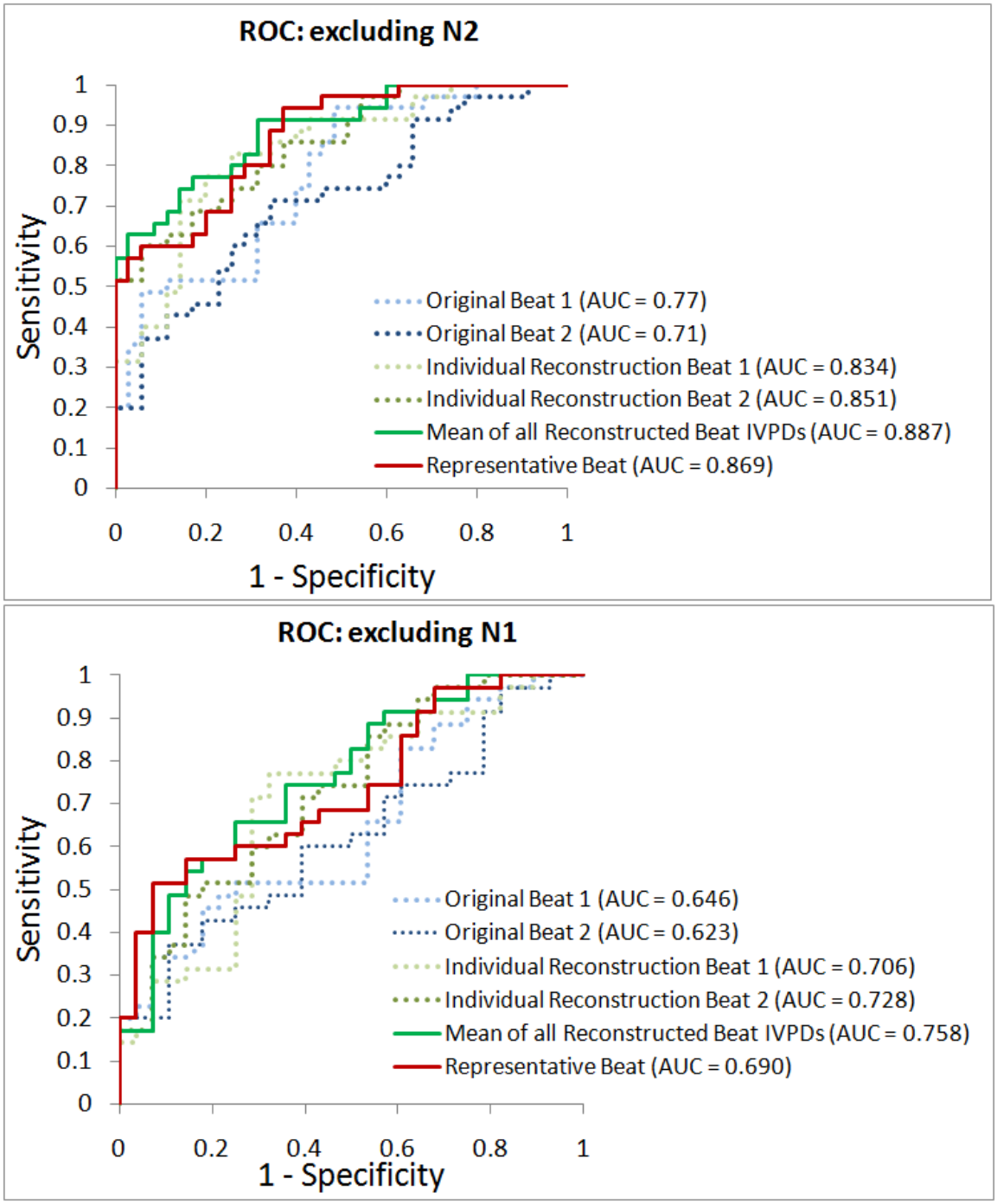

Figure 2.8: Receiver operator characteristic curves for two groupings of clinical cohort patients. Both plots show an improved area under the curve (AUC) for the mean of all reconstructed beat IVPDs and the representative beat IVPD when compared with the original beats.

2.5 Discussion

2.5.1 Current IVPD Limitations

To date very little has been done to investigate effects of scanner settings and beat-to-beat variations on the resulting IVPD values. It has been shown that error bounds on Doppler derived indices may increase in low resolution images (*18*), but no work has been done to correct this issue, or document its relevance on clinical data. Beat-to-beat variation and the effects of scan-line alignment have also been investigated previously (*19, 20*). It has been shown that misalignments in the transducer scan-line, up to 20 degrees, result in small changes in calculated IVPD, ~0.26 mmHg. Scan line misalignment may account for some scatter seen in beats from the same patient, and also motivates the development of a reconstructed beat which is representative of velocity information from multiple beats. These two issues, a strong dependence of IVPD on sweep speed and beat-to-beat variations caused by signal artifacts, patient motion, and scan-line alignment, must be addressed before IVPD has robust clinical utility. Using the proof of concept cohort we showed that the IVPD estimation is highly dependent on the scanner sweep speed setting and hence the temporal resolution of the scan (Figure 2.6). The highest resolution scan returns a reasonable value for a normal subject, but all beats in the 25 mmps group and several in the 50 mmps group would classify the first two normal subjects as diseased. A value of 2.2 mmHg has previously been used as diseased value to classify patients with dilated cardiomyopathy (*21*) and can be used as a reference value in this work as well. This is not used as a cutoff value as dilated cardiomyopathy can be considered a worst case for suction generation. The reduced IVPD in the low sweep speed groups is due to the insufficient sampling rate. As a result, scans analyzed at the lowest sweep speeds could potentially be misdiagnosed, compromising the clinical utility of IVPD.

2.5.2 Addressing Current Limitations with Spatiotemporal Reconstruction

Using the POD reconstruction method developed here, all of the originally lower resolution groups (25 mmps, 50 mmps, 75 mmps, and 100 mmps) were reconstructed to 1.9 ms/pix (Figure 2.6). All of the resolution groups show median values above 2.2

mmHg after the POD interpolation and would classify this subject as normal. This illustrates that by reconstructing all echocardiograms at a higher resolution, we are capable of rectifying any echocardiogram to return an IVPD value similar to what would have been measured if the scan had been recorded at the highest sweep speed. This can lead to less mis-classification and improved clinical utility.

Moreover because the POD captures the common modes between all available heartbeats (*22*) these POD modes can be used to reconstruct a representative beat. The significance of the representative heartbeat is that common signal structures observed in all heartbeats are present in the reconstruction. However, any differences which may arise from transducer motion, patient motion, noise or signal artifacts, are removed from the reconstructed signal. This reduces the chance of having an erroneous IVPD measurement due to only analyzing a single heartbeat. Analyzing a representative beat which contains common information between a series of beats yields a more comprehensive picture of that specific patient's filling pattern and is less prone to inaccurate IVPD measurements.

All heartbeats from proof of concept cohort were reconstructed to all observed scanner resolutions, and also to two higher resolutions, 1.4 ms/pix and 0.95 ms/pix in order to explore the limits above which the results become independent of the sampling rate. The IVPD values appear to converge to a pressure value at the highest scanner resolution of (1.9 ms/pix, 2.6 ms/pix and 1.6 ms/pix) and remain almost constant. Although the higher sampling rate shows similar IVPD values they are subject to increased noise as is shown by the increased interquartile range (Figure 2.7). This suggests that at a certain point, the reconstruction begins introducing more noise into the image. For these reasons, a scan resolution of 1.9 ms/pix was used to analyze the clinical cohort.

2.5.3 Clinical Cohort shows Improved Clinical Utility

The method was demonstrated using five clinical sub-cohorts, which were analyzed to show how the POD reconstruction affected IVPD values in clinical images with only 2-3 beats available for analysis. Prior to reconstruction, sub-cohorts N2 and N3 would both, most likely, be classified as diseased based on the low IVPD values (2.29 mmHg and 1.77 mmHg respectively). After reconstruction, these sub-cohorts returned

IVPD values of 3.41 mmHg and 3.09 mmHg respectively, consistent with the expected normal ranges. This shows that the method is capable of improving low resolution scans to obtain better measurements. The two diseased cohorts, R1 and LVH, also show an increase in IVPD after interpolation, but still remain in diseased filling ranges (2.28 mmHg to 2.89 mmHg and 1.45 mmHg to 2.27 mmHg respectively). The representative beats for all patient groups return a median IVPD value similar to the median of all individual reconstructed beats as expected. This shows that the representative reconstructed beat is capable of generating a good description of the LV filling wave, while reducing erroneous measurements incurred by beat-to-beat variations.

Receiver Operator Characteristic (ROC) curves are commonly used to rate the clinical utility of a diagnostic parameter. In this work, each normal and diseased sub-cohort combination (R1 and N1, N2, N3; LVH and N1, N2, N3) was used to test the clinical utility of the reconstructed IVPD measurement. The AUC for all sub-cohort combinations and all parameters are summarized in Table 2.4. There are three important things we learn from this analysis.

First, in sub-cohort combinations where the diseased group was recorded at a low resolution and the normal group was recorded at a high resolution (LVH and N1; LVH and N2), we see very little effect of the methodology on the AUC. This is because there is an inherent flaw in how the data was recorded. The original analysis will perform well in this scenario because all diseased patients automatically have lower IVPDs due to the lower quality scan. In these sub-cohort combinations, there is little effect on the AUC, but there is an overall increase in IVPD values as shown from the results inTable 2.3.

Second, when a sub-cohort combination had a normal cohort and a diseased cohort with comparable resolutions (N1 and R1, N2 and R1, N3 and LVH), the AUC increased for the representative beat and the mean of all individual reconstructed beats over the AUC for the original beats. This shows that even in relatively high resolution scans, we can obtain additional information through the POD spatiotemporal reconstruction.

Third, and perhaps most importantly, in the sub-cohort combination where the normal cohort had a low resolution and the diseased cohort had a high resolution (N3 and R1), the original beat analysis shows an AUC less than 0.50. In this particular sub-cohort

combination, the diseased patients are showing higher IVPDs than the normal patients. Having no prior knowledge of the clinical classification of these patients, the IVPD parameter would most likely mis-classify all patients. After the reconstruction, the individual reconstructed beats, the mean of all individual reconstructed beats, and the representative beats are showing improved clinical utility are AUCs greater than 0.50, meaning the reconstruction was able to reverse the incorrect trend observed in the original analysis and return more accurate IVPD values.

A Tukey-Kramer HSD test was applied to determine if sub-cohort combinations were statistically different. The test was applied to the same parameters as the ROC analysis above, including individual original beats, individual reconstructed beats, the mean of all individual reconstructed beats, and the representative beat. The reconstruction parameters showed improved ability to differentiate between the normal sub-cohorts and the diseased sub-cohorts after reconstruction. Both the mean of all reconstructed beats and the representative beat correctly pair five out of six groupings, whereas the two individual original beats only correctly differentiate three out of six and two out of six. The Tukey-Kramer test was also applied to all normal cohorts to determine if they are statistically similar. After reconstruction, we see a slight improvement in grouping normal sub-cohorts with other normal sub-cohorts.

Two larger patient groups were formed from the sub-cohorts (Figure 2.8). These groupings were formed to keep the numbers of normal and diseased patients in each group as even as possible. In both of the patient groupings there is an increase in the AUC for the representative beat and the mean of all reconstructed beats when compared to the original beats. This supports what was observed in the sub-cohort pairings, that the reconstruction improves the scan quality and allows for improved IVPD measurements with no dependence on the scanner acquisition settings.

2.5.4 Limitations

There are several limitations which must be addressed. First, the effect of reconstruction and the introduction of noise into the image must be better understood. One goal of this work was to improve resolution while decreasing noise in the image. It is clear, however, that at some point when reconstructing to the highest resolutions, noise can be added to the image. The ideal reconstruction resolution must be determined.

In addition, this methodology should be applied to a larger cohort including patients recorded on a wide range of machines across many scanner acquisition settings. Only then can we reliably confirm the improved clinical utility of the IVPD parameter after spatiotemporal reconstruction.

2.6 Conclusions

A new methodology has been presented which is capable of reconstructing CMM echocardiograms recorded at low sweep speeds to higher temporal resolutions, while controlling the noise in the resulting image. This allows for a universal framework to enhance CMM data, improving the derived IVPD as a diagnostic parameter, allowing for independence from scanner acquisition settings, and improving the clinical utility of this parameter. Never before have these limitations of IVPD been addressed or corrected. The potential of IVPD as a diagnostic parameter is dependent on reliable and accurate measurement, and this work presents a framework for rectifying all CMM echocardiograms to a quality image which can be analyzed to obtain the necessary reliable measurements, whether it be on an individual single beat, or a representative beat, synthesizing velocity information from any number of available heartbeats.

2.7 References

1. N. L. Greenberg, P. M. Vandervoort, J. D. Thomas, Instantaneous diastolic transmitral pressure differences from color Doppler M mode echocardiography. *Am. J. Physiol.-Heart Circul. Physiol.* **271**, H1267 (Oct, 1996).
2. R. Yotti *et al.*, A noninvasive method for assessing impaired diastolic suction in patients with dilated cardiomyopathy. *Circulation* **112**, 2921 (Nov, 2005).
3. A. Rovner *et al.*, Improvement in diastolic intraventricular pressure gradients in patients with HOCM after ethanol septal reduction. *American Journal of Physiology - Heart and Circulatory Physiology* **285**, H2492 (December 1, 2003, 2003).
4. T. E. Claessens, J. De Sutter, D. Vanhercke, P. Segers, P. R. Verdonck, New echocardiographic applications for assessing global left ventricular diastolic function. *Ultrasound Med. Biol.* **33**, 823 (Jun, 2007).
5. W. C. Little, Diastolic dysfunction beyond distensibility - Adverse effects of ventricular dilatation. *Circulation* **112**, 2888 (Nov, 2005).

6. S. F. Nagueh *et al.*, Recommendations for the Evaluation of Left Ventricular Diastolic Function by Echocardiography. *Eur. J. Echocardiogr.* **10**, 165 (March 1, 2009, 2009).
7. R. M. Lang *et al.*, Recommendations for Chamber Quantification: A Report from the American Society of Echocardiography's Guidelines and Standards Committee and the Chamber Quantification Writing Group, Developed in Conjunction with the European Association of Echocardiography, a Branch of the European Society of Cardiology. *Journal of the American Society of Echocardiography* **18**, 1440 (2005).
8. R. D. Mosteller, Simplified calculation of body-surface area. *The New England journal of medicine* **317**, 1098 (1987).
9. R. B. Devereux *et al.*, Echocardiographic assessment of left ventricular hypertrophy: Comparison to necropsy findings. *The American Journal of Cardiology* **57**, 450 (1986).
10. M. S. Firstenberg *et al.*, Noninvasive estimation of transmitral pressure drop across the normal mitral valve in humans: importance of convective and inertial forces during left ventricular filling. *J Am Coll Cardiol* **36**, 1942 (November 15, 2000, 2000).
11. K. C. Stewart *et al.*, Evaluation of LV Diastolic Function From Color M-Mode Echocardiography. *JACC: Cardiovascular Imaging* **4**, 37 (2011).
12. G. Berkooz, The Proper Orthogonal Decomposition in the Analysis of Turbulent Flows. *Annu. Rev. Fluid Mech.* **25**, 539 (1993).
13. L. Sirovich, Chaotic dynamics of coherent structures. *Physica. D* **37**, 126 (1989).
14. T. R. Smith, Low-Dimensional Modelling of Turbulence Using the Proper Orthogonal Decomposition: A Tutorial. *Nonlinear dynamics* **41**, 275 (2005).
15. N. Aubry, Spatiotemporal analysis of complex signals: Theory and applications. *Journal of statistical physics* **64**, 683 (1991).
16. D. V. Hinkley, Inference about the Change-Point from Cumulative Sum Tests. *Biometrika* **58**, 509 (1971).
17. W. A. Taylor. (2000), vol. 2008.
18. J. L. Rojo-Álvarez *et al.*, Impact of image spatial, temporal, and velocity resolutions on cardiovascular indices derived from color-Doppler echocardiography. *Medical Image Analysis* **11**, 513 (2007).
19. N. L. Greenberg, S. Krucinski, P. M. Vandervoort, J. D. Thomas, Importance of scanline orientation for color Doppler M-mode diastolic inflow patterns and pressure gradient calculations. *J. Am. Coll. Cardiol.* **29**, 49166 (Feb, 1997).
20. N. L. Greenberg, P. M. Vandervoort, M. S. Firstenberg, M. J. Garcia, J. D. Thomas, Estimation of diastolic intraventricular pressure gradients by Doppler M-mode echocardiography. *Am. J. Physiol.-Heart Circul. Physiol.* **280**, H2507 (Jun, 2001).
21. R. Yotti *et al.*, Doppler-Derived Ejection Intraventricular Pressure Gradients Provide a Reliable Assessment of Left Ventricular Systolic Chamber Function. *Circulation* **112**, 1771 (September 20, 2005, 2005).
22. J. Kriegseis, Common-base proper orthogonal decomposition as a means of quantitative data comparison. *Measurement science & technology* **21**, 085403 (2010).

3. Dispersive Behavior of LV Filling Waves

Casandra Niebel[1] , William Little[2,] Pavlos Vlachos[1],

[1]Department of Mechanical Engineering, Virginia Tech, Blacksburg VA

[2]Cardiology Section, Wake Forest Univ. Baptist Medical Center, Winston-Salem NC

3.1 Abstract

Heart failure is a progressive disease which changes the loading conditions on the heart. Altered pressure or volume loading causes the myocardial wall to remodel, changing the structure and functional properties of the left ventricle, resulting in systolic heart failure, diastolic dysfunction, or a combination of both. In this work we analyzed Color M-Mode echocardiograms of normal and diseased subjects and discovered that ventricle filling waves are dispersive and consist of many wave components propagating at different propagation velocities. The propagation of each individual wave component can be measured using a continuous wavelet transform analysis and can be used to calculate a dispersion rate. The dispersion rate captures the degree of dispersion and is found to depend on the progression of myocardial remodeling, with normal elliptical ventricles displaying high dispersion, hypertrophied ventricles displaying lower dispersion and dilated cardiomyopathy ventricles displaying low dispersion. This dispersion rate and the propagation velocity of energetically dominant wavenumbers are proposed as improved parameters to measure the early diastolic filling wave propagation velocity.

3.2 Introduction

3.2.1 Heart Failure and Left Ventricle Remodeling

Heart failure is a progressive disease which affects loading conditions on the heart, reducing heart function, modifying chamber geometry, and changing mitral inflow

patterns (*1, 2*). Traditionally heart failure was perceived as a loss of systolic function evident by a reduced ejection fraction, but recent studies have shown that left ventricular diastolic dysfunction (LVDD) exists independent of systolic failure and has a similar prognosis. LVDD is any abnormality in left ventricle mechanical function during diastole and is characterized by increased myocardial stiffness and impaired relaxation (*3*). Despite the prevalence of LVDD, affecting all heart failure patients and approximately 50% of those with preserved systolic function (*4-6*), there is no diagnostic gold-standard and there is a limited understanding of the physical parameters that govern LV filling.

In diseased hearts, myocytes either become thicker, in which case the LV hypertrophies, or elongate, causing LV dilation, both in an attempt to compensate for the increased loading on the heart. Initially this adaptive response improves heart function, but progression of the disease leads to a continuation of LV remodeling, LVDD, or systolic heart failure (*7*). In this work, we analyze mitral inflow in normal ventricles, hypertrophied ventricles, and dilated ventricles to further understand the effect of the myocardial wall remodeling in the LV filling process.

3.2.2 Color M-Mode Echocardiography and Conventional Propagation Velocity (V_P)

LV filling is imaged using CMM echocardiography which records a spatiotemporal map of blood velocity propagating along a scan-line from the mitral valve towards the apex. The filling wave, recorded by CMM, is conventionally used to qualitatively assess LV function and manually measure a wave propagation velocity (V_P). The V_P is defined as the slope of the first aliasing boundary (yellow to blue transition) from the mitral plane to a distance 4 cm into the LV (*8*). The current methodology makes several assumptions about the nature of the filling wave. First it assumes that the filling wave is constant and is best represented by a single linear slope. However, previous studies have shown that the leading edge of the wave can be curvilinear (*9*), or that the propagation velocity is better represented by two slopes, corresponding to an initial and a terminal V_P (*10*). Second, the current methodology assumes that the user-selected aliasing boundary, during image acquisition, will correspond to the velocity magnitude

that better captures the V_P. However, when different aliasing boundaries were tested (*11*, *12*), corresponding to different iso-velocity contours, the resulting V_P varied greatly (*13*, *14*). As shown in Figure 3.1, there is significant variation in the leading edge slope for various iso-velocities. The 10% contour propagates more rapidly, as indicated by the green line, than the 75% contour as indicated by the red line. The third assumption is that that the wave moves with a constant velocity hence tracking a single iso-velocity is representative of the V_P. In other words this assumes that the LV filling wave propagates as a constant wavefront. However, the dependence of V_P on iso-velocity indicates that the filling wave is composed of multiple wave components, each propagating with different velocity. This wave behavior is referred to as dispersive and will be further explained in the next section. Clinically, this challenges the physical relevance of conventional V_P since it fails to capture an important characteristic and could potentially limit diagnostic ability.

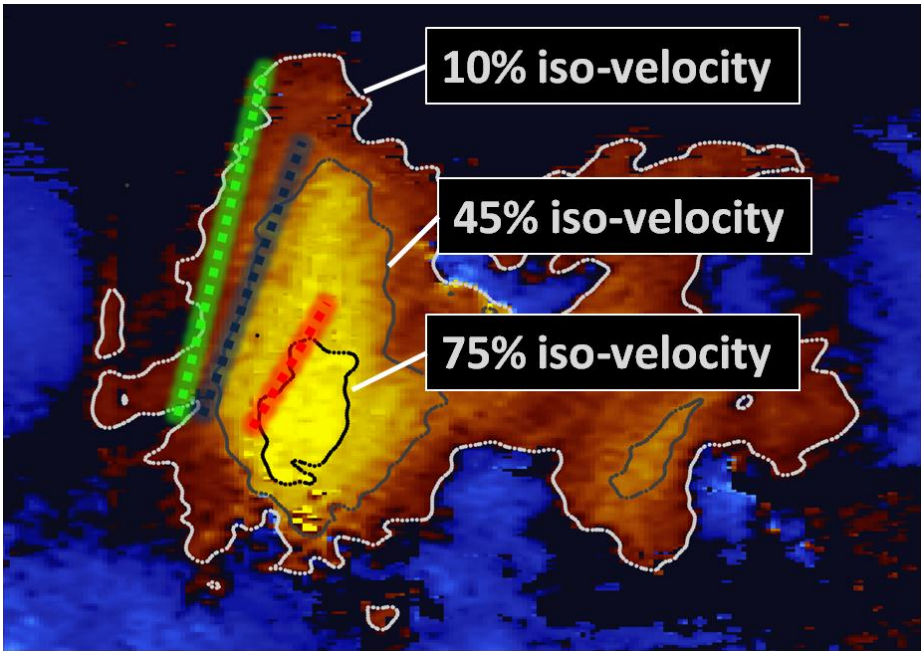

Figure 3.1: An example CMM echocardiogram showing the dependence of conventional propagation velocity on the choice of iso-velocity contour. The green line follows the motion of the 10% iso-velocity contour and is moving much more rapidly than the red line which is following the motion of the 75% iso-velocity contour. This motivates moving away from iso-velocity assumptions and tracking the true wave.

3.2.3 Dispersive and Non-Dispersive Waves

A dispersive wave is a wave consisting of many wave components, propagating at different velocities (*15*). A wave can be made up of many wave components, all with a unique wavenumber and magnitude, which propagate with the wave. If all components propagate at the same velocity, the wave is non-dispersive, whereas if the wave components propagate at different velocities, the wave is dispersive. Proper quantification of a dispersive wave requires taking into account the motion of all wave components. In this work we use a dispersion rate which is the rate at which the propagation velocity changes as a function of wavenumber (or spatial frequency of one wave component) (*15*).

It is important to note that dispersion does not necessarily correspond to a loss of energy or a convective spreading of the flow. Within the context of this analysis when looking at the LV filling wave, dispersion is not a spreading of the mitral inflow jet radially away from the center of the LV. Previous work has shown that convective deceleration is detrimental to the LV filling (*16*) and this is not what the dispersion rate is capturing.

The term, "dispersion", has been used previously to describe early diastolic filling waves measured using mitral inflow Doppler (*17-19*). The peak mitral inflow velocity during the E-wave was recorded simultaneously at 1cm, 2cm, and 3cm downstream from the mitral plane. The ratio of the peak mitral inflow velocity at 3 cm to the peak mitral inflow velocity at 1 cm was reported as the intra ventricular dispersion. These groups found a decreased ratio of regional peak velocities in several diseased groups. While this reported ratio shows changes in filling wave dynamics in health and disease, it does not calculate a physical dispersion rate or describe how the various wave components are propagating in relation to one another. This intra-ventricular "dispersion" is more likely capturing a dissipation of wave energy by observing a lower velocity as the wave propagates further into the LV.

In this work we analyze all velocity information available within the CMM scans. In doing so, we remove the first and second assumptions with respect to the V_P

estimation by no longer measuring a slope based on an iso-velocity contour and instead calculate a new V_P that is not subject to subjective selection of iso-velocity contours. In addition, we directly challenge the third assumption by hypothesizing that the LV filling wave is not a bulk wave moving with a constant velocity but instead is a dispersive wave and that the dispersion rate is affected by geometry changes in the left ventricle.

3.3 Methods

3.3.1 CMM Acquisition and Patient Cohorts

Echo Doppler examinations were completed using an iE33 (Philips Medical Systems, Andover, Massachusetts) and a multiple frequency transducer. CMM echocardiograms were recorded in the apical long axis view with a color scale that optimized visualization as judged by the recording sonographer. Three independent patient cohorts were used in this analysis. A normal cohort consists of 36 patients diagnosed as having a normal filling pattern based on peak early filling mitral inflow velocity, tissue Doppler mitral annular velocities and conventional propagation velocity, as recommended by the American Society of Echocardiography guidelines. A second cohort consisted of 9 patients diagnosed with severe LV hypertrophy. LVH is indicated by an elevated LV mass index, or the ratio of LV mass to body surface area (*20*). A third cohort consisted of 15 patients with dilated ventricles. These patients were diagnosed with dilated cardiomyopathy based on a reduced sphericity index (*21*) and a reduced ejection fraction. Cohort details are recorded in Table 3.1. Patients were all undergoing clinically indicated echocardiography at the Wake Forest University Baptist Medical Center. The study was conducted according to protocols approved by the Virginia Tech and Wake Forest University Baptist Medical Center institutional review boards.

Table 3.1: Clinical details for the three patient cohorts.

Group	N	Age		Ejection Fraction		Geometry Classifier
		Median	IQR	Median	IQR	
Normal	36	30	25-49	60	55-63	Na
DCM	15	58	53-68	20	15-25	SI < 1.60
LVH	9	60	64-73	16	15-22	LVMI > 175

Values reported are median and interquartile range (25% - 75%)
DCM – Dilated Cardiomyopathy
LVH – Left Ventricular Hypertrophy

3.3.2 Dispersion Rate

A dispersion rate describes the relationship between propagation velocity and wavenumber, k. In this work, a slope is fit to model the relationship between propagation velocity andwavenumber. If all wavenumbers propagate at approximately the same velocity, the dispersion rate is approximately zero and the wave is considered non-dispersive. If the wavenumbers are propagating at different velocities, this is a dispersive wave. To calculate a dispersion rate, it is necessary to know all wave components in the wave. To measure the propagation velocity of each wave component, we must know the spatial location of each component as a function of time. Fourier methods are typically used to identify what wavenumbers are present in a signal. A Fourier transform does not provide spatial or temporal localization of each wavenumber. A continuous wavelet transform, which is described in detail in the following section, provides spatial and temporal localization of all wavenumbers, allowing us to calculate a new V_P independent of iso-velocity assumptions, and also a V_P for each wave component, allowing for the calculation of a dispersion rate.

3.3.3 Continuous Wavelet Transform

The continuous wavelet transform, Equation 3-1, convolves a signal $f(x)$ with a series of scaled and translated continuous wavelet functions,$\psi(\frac{x-b}{a})$, to reveal signal energy as a function of space and wavenumber. The scaling of this continuous function,a, stretches or compresses the wavelet function and provides frequency

localization. A stretched wavelet will become longer spatially, and will capture the energy of low wavenumber components. A compressed wavelet will become shorter spatially and will capture the energy of high wavenumber components. The translation parameter of this function, b, provides spatial localization and shifts each wavelet along the entire length of the signal. The results of a CWT are dependent on the appropriate choice of mother wavelet and the appropriate choice of scales. Before we could proceed, we had to determine these two factors.

$$W_T(a,b) = a^{-1/2} \int f(x) * \psi\left(\frac{x-b}{a}\right) dx \qquad \textbf{3-1}$$

3.3.3.1 Complex Morlet Wavelet

For this work, the complex Morlet wavelet was chosen as the mother wavelet. The Morlet wavelet, Equation 3-2, is essentially a sine wave modulated by a Gaussian window, and has been used previously in biological applications due to its smooth continuous oscillations (*22*). In addition, the Morlet wavelet provides high control over the resulting frequency spectrum of the scaled and translated wavelets.

$$\Psi(x) = \frac{1}{\sqrt{\pi f_b}} e^{i2\pi f_o x} e^{\frac{-x^2}{f_b}} \qquad \textbf{3-2}$$

Two parameters govern the Morlet wavelet, first, a frequency parameter, f_o, which defines the frequency of the sine wave component and second, a bandwidth parameter, f_b, which defines the bandwidth of the Gaussian modulating window. By controlling these two parameters, any number of mother wavelets can be generated, with the stipulation that the wavelet function must have near zero mean (~5-7 oscillations) and have endpoints with zero magnitude (*23*, *24*).

3.3.3.1.1 Optimizing Morlet Wavelet Parameters

The frequency parameter and the bandwidth parameter are linked together based on the total number of oscillations in the resulting mother wavelet. A higher frequency wavelet with a wide bandwidth will have many oscillations whereas a mother wavelet with a lower frequency and a narrow bandwidth will have fewer oscillations and may not meet the condition to have zero mean. The input parameters are related by the following relationship.

$$f_b = \frac{n_{cycles}}{2\pi f_o} \qquad \textbf{3-3}$$

An optimum Morlet wavelet can be determined by optimizing either the bandwidth parameter or the frequency parameter and solving for the other parameter based on the desired number of oscillations. In this work, we chose to optimize the frequency parameter and then solve for a bandwidth parameter to maintain 6 oscillations in the mother wavelet function.

Before choosing a frequency parameter, it is necessary to have a good idea of how much of the signal represents the true flow and how much of the signal is noise or artifacts from the image acquisition process.

3.3.3.1.1.1 Proper Orthogonal Decomposition to estimate SNR

A Proper Orthogonal Decomposition, or POD, is a technique commonly used in signal processing to decompose a signal into a series of basis functions; each of which contains a certain percentage of the original signal energy (*25, 26*). The original signal can then be recovered, or, a subset of the basis functions can be chosen to reconstruct a signal with less noise and irregularities, using Equation 3-4 where $\emptyset_k$ are the basis functions and α_k are mode coefficients. Each mode has a corresponding eigenvalue, λ_k, which reveals how much of the original signal energy that mode contains.

$$v(x,t) = \sum_{k=1}^{N} k(t)\varphi_k(x) \qquad \textbf{3-4}$$

POD mode entropy is often used to determine how many modes, or basis functions to retain in the reconstruction and how many to discard (*27*). Below, p_k represents the normalized energy of each mode, K is the total number of modes, and H_k is the mode entropy (*27*) .

$$p_k = \frac{\lambda_k^2}{\Sigma \lambda_k^2} \qquad \textbf{3-5}$$

$$H_k = -\frac{1}{\log(K)} \sum_{k=1}^{K} p_k log(p_k) \qquad \textbf{3-6}$$

As the POD mode entropy spectrum reaches a plateau it signifies that all prior basis functions contain all significant information. Any subsequent modes contribute to noise. To locate this plateau point, a change point analysis was utilized (*28*), as defined in Equation 3-7.

$$Cumulative\ Sum_k = Cumulative\ Sum_{k-1} + (H_k - \overline{H}) \qquad \textbf{3-7}$$

A first estimate of signal is reconstructed using all basis functions prior to the plateau point. A first estimate of the noise in the signal is calculated by subtracting the first estimate of signal from the original signal as stated in Equation 3-8 and shown in Figure 3.2.

$$u_{noise}(y,t) = u_{received}(y,t) - u_{reconstructed}(y,t) \qquad \textbf{3-8}$$

It is important here to note, that this provides only an estimate of signal and noise. The purpose of this step was to obtain an initial estimate of signal to noise ratio which we can use to find a frequency parameter which optimizes the SNR.

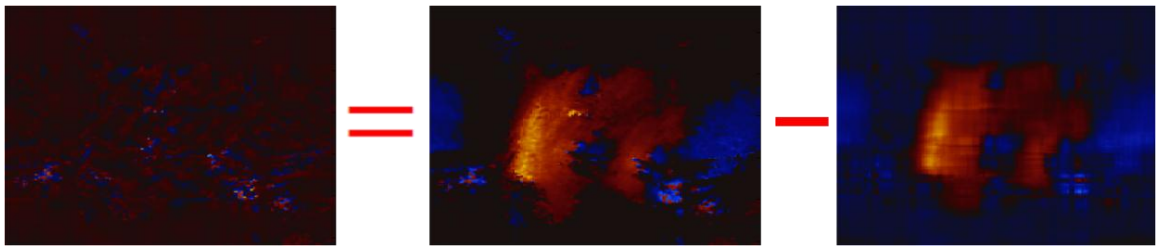

Figure 3.2: Illustration of the estimation of $u_{noise}(y,t)$ from $u_{received}(y,t)$and $u_{reconstructed}(y,t)$. $u_{reconstructed}(y,t)$ and $u_{noise}(y,t)$ are used as an initial estimation of "Signal" and "Noise".

3.3.3.1.1.2 Gaussian Pseudo Filter to optimize SNR

After having determined a first estimate of signal and noise, we can use, $u_{reconstructed}(y,t)$ and $u_{noise}(y,t)$ to calculate the SNR of the received velocity field. By applying a Gaussian pseudo filter to the reconstructed signal and noise, and incrementally increasing the cutoff wavenumber, we can obtain the signal to noise ratio as a function of the filter cutoff as shown in Equation 3-9. This is named a "pseudo" filter because it is not actually being used to filter the data. Instead, just the SNR of the resulting signal (if the filter had been applied) is calculated.

$$SNR(F_c) = \frac{2\left[\int_0^{F_c} |U_{reconstructed}(f)|\,df\right]^2}{\int_0^{F_c} (U_{noise}(f) \cdot U_{noise}(f)^*)\,df} \qquad \textbf{3-9}$$

Where $U_{reconstructed}(f)$ and $U_{noise}(f)$, are the Fourier Transform of $u_{reconstructed}(y)$ and $u_{noise}(y)$, and * indicates the complex conjugate. F_c is the filter cutoff wavenumber which is initially set to include only the first wavenumber and is incrementally increased to include all wavenumbers. The cutoff wavenumber which maximizes the SNR is used to define the optimal mother wavelet center frequency.

3.3.3.2 Scaling Function

The minimum wavenumber of interest is set to the minimum resolvable wavenumber from the CMM echocardiogram or, the inverse of the physical length of the CMM image. The maximum wavenumber to scale the mother wavelet is set to the wavenumber which maximized the SNR in the previous step. One hundred equally spaced scaling factors are generated to scale the mother wavelet from the minimum wavenumber to the maximum wavenumber.

3.3.4 Calculating Dispersion Rate

After the optimal mother wavelet is generated, it is scaled to all applicable wavenumbers and translated to all spatial locations. This family of wavelets is used to apply the continuous wavelet transform to the data. The result of the CWT applied to this spatiotemporal map of velocity values is a three dimensional CWT power spectra, localized in space, time, and wavenumber as shown in Figure 3.3. The spatial lag of each wavenumber can be calculated between two time steps using a phase only cross correlation, Equation 3-10 , where V_1 and V_2 are the Fourier transform of the two spatial velocity signals at time t_1 and time t_2 and '*' indicates complex conjugate. The spatial lag is measured by locating the maximum on the cross correlation, r. This spatial lag and the known time difference between the two time steps can be used to calculate a propagation velocity corresponding to each wavenumber, $V_{P,k}$.

$$r = \mathcal{F}^{-1}\left[\frac{V_1 V_2^*}{|V_1 V_2^*|}\right] \qquad \textbf{3-10}$$

To calculate a dispersion rate, we first want to locate which wavenumbers are the most energetically dominant. To do this, the normalized CWT power spectrum as a function of wavenumber was calculated. The wavenumber at which this normalized CWT power spectrum drops below 25% of the maximum is used as the cutoff for dominant wavenumbers. The dispersion rate is calculated by fitting a linear slope to the

$V_{P,\,k}$ versus dominant wavenumbers relationship. The slope of this fit is reported as the dispersion rate.

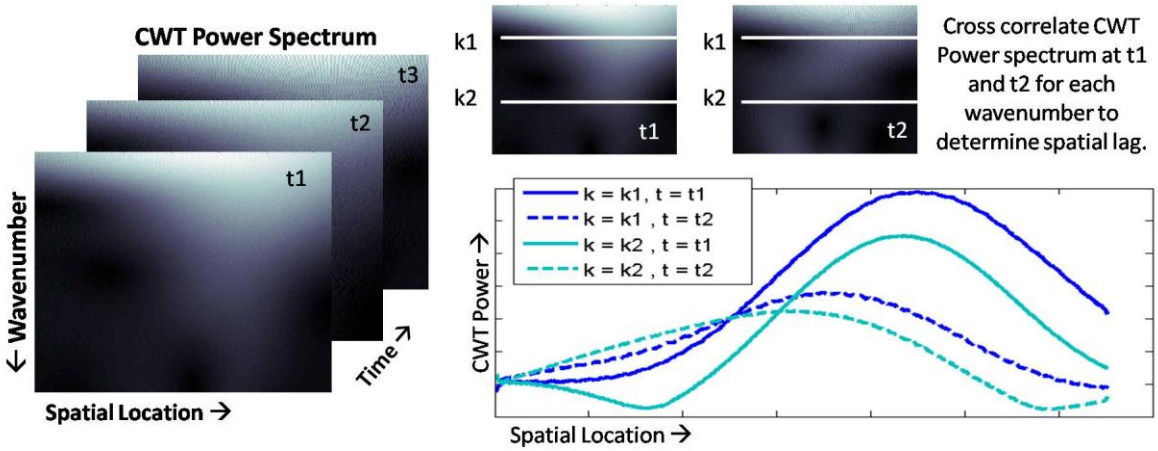

Figure 3.3: Calculation of the Dispersion Rate. Far left, and example of the CWT power spectra localized in space, time, and wavenumber. The motion of the peaks is tracked between two time steps using a cross correlation at each wavenumber. Two example wave numbers are plotted in the lower right. The solid lines represent t1 and the dashed lines represent t2 for the two wavenumbers k1 and k2.

3.3.5 Doppler Derived IVPD

A Doppler-derived intra ventricular pressure difference (IVPD) can be measured using the CMM echocardiogram velocity data to solve the Euler equation (*16*, *29*).

$$\frac{\partial P}{\partial x} = -\rho\left[\frac{\partial U}{\partial t} + U\frac{\partial U}{\partial x}\right] \qquad \textbf{3-11}$$

where U is velocity, P is pressure and ρ is the density of blood. Spatial and temporal derivatives are calculated and used to solve for $\frac{\partial P}{\partial x}$. The line integral along the length of the ventricle is calculated at each time step, yielding a spatio-temporal profile of pressure values $P(x,t)$. A temporal profile of IVPD is calculated by subtracting the pressure at the mitral valve from the pressure at the apex. The peak IVPD during early filling is then

identified. This method has been validated with comparisons to direct invasive pressure measurements by micro manometers (*16, 30, 31*).

3.3.7 Conventional V_P and V_S

The conventional V_P parameter, measuring the slope of the 50% iso-velocity contour (*32*) was automatically calculated using an in-house algorithm (*10*). Also, the filling strength parameter, or V_S, was calculated using this same algorithm. An ensemble contour is generated and a breakpoint is located. The product of the initial propagation velocity and the distance to which this velocity extends into the LV is the filling strength. Details describing the calculation of V_S and its clinical utility are in (*10*).

3.4 Results

3.4.1 Representative Patients

The analysis was applied to three patient cohorts including normal elliptical ventricles (n = 26), hypertrophied ventricles (n = 9) and dilated ventricles (n = 15). One representative patient from each cohort was chosen to demonstrate the changes in dispersive wave behavior. The top row of Figure 3.4 shows a representative normal patient. The CWT is applied to each spatial velocity signal on the CMM echocardiogram resulting in a CWT power spectrum localized in space, time and wavenumber. The spatial lag of the peak on the CWT power spectra is calculated between two time steps, for each wavenumber (horizontal location). The spatial lag and the time between the two time signals are used to calculate a propagation velocity for each wavenumber. The slope describing the relationship between wavenumber and propagation velocity is reported as the dispersion rate. The maximum V_P and the mean V_P are also recorded for analysis. As is evident from the CWT images, the higher wavenumbers have higher displacements than the lower wave numbers. The dispersion rate for the normal patient example is 212.23 cm^2/s, and is plotted in blue in the bottom plot of Figure 3.4.

The second example in Figure 3.4 shows a representative patient from the hypertrophied cohort. This patient was diagnosed as having left ventricular hypertrophy (LVH) based on an elevated left ventricular mass index (LVMI), or ratio of LV mass to body surface area (*20, 33, 34*). The two spatial velocity signals of interest are plotted as the vertical blue lines overlaid on the CMM echocardiogram. The CWT power spectra also show an increased propagation of the higher wave numbers as compared to the lower wave numbers. The dispersion rate for this specific LVH patient is 93.23 cm^2/s and is plotted in green in Figure 3.4. This specific LVH patient has a reduced dispersion rate from the normal patient but still displays dispersive characteristics.

The third patient in Figure 3.4 is a representative patient from the dilated cohort. This specific patient was diagnosed with Dilated Cardiomyopathy (DCM) due to a decreased sphericity index, or the ratio of LV length to LV width (*21*), and a reduced ejection fraction. The CWT power spectra show that each wave number moves approximately the same distance, indicating a relatively constant propagation velocity across all wave numbers. The dispersion rate for this patient is 5.28 cm^2/s and is plotted in purple on Figure 3.4. The low dispersion rate indicates that this wave is non-dispersive and moves as a bulk flow wave.

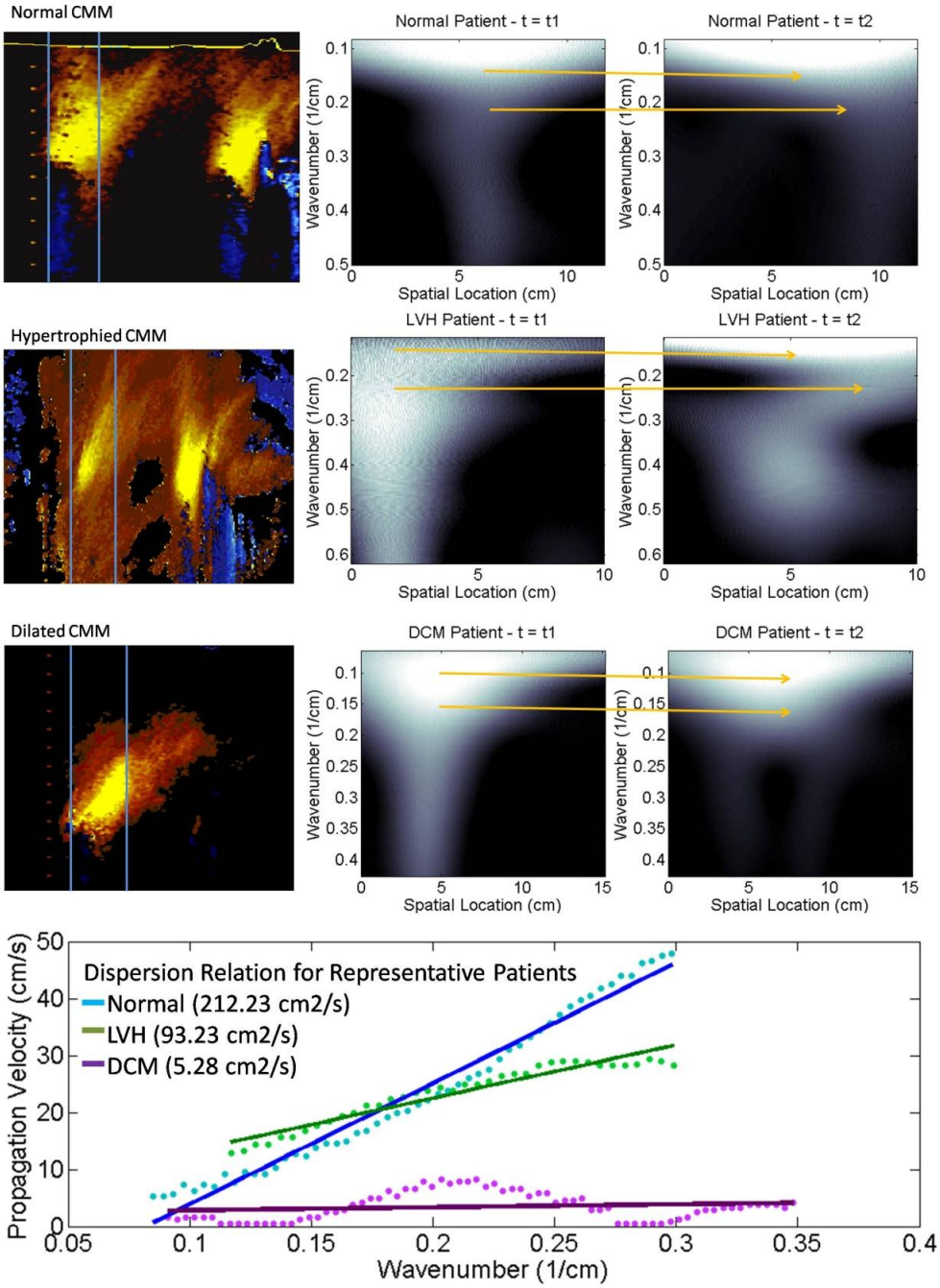

Figure 3.4: Representative patients from the dispersion rate analysis. Top, normal filling pattern; Center, hypertrophied filling; Bottom, dilated. The first column shows the CMM echocardiogram for each representative patient with t1 and t2 indicated by the vertical blue lines. The next two columns show the CWT power spectra at t1 and at t2. The yellow lines animate the motion of the peaks. The bottom plot shows the dispersion rate for each of these patients plotted over only the dominant wavenumbers.

The range of wave numbers over which the dispersion rate is calculated is dependent on each CMM echocardiogram and the range of dominant wavenumbers is specific to each patient. The minimum wave number considered is the inverse of the physical length of the LV. The LVH representative patient image has a physical height of 8.2 cm, while the DCM patient and Normal filling patient have physical heights of 9.6 cm and 10.7 cm respectively. These heights correspond to minimum wavenumbers of 0.12 /cm, 0.100 /cm, and 0.098 /cm for the LVH, DCM, and normal representative patients. The maximum wavenumber is also specific to each patient and is dependent on the most energetic wave components present in each signal.

3.4.2 Estimation of Conventional Parameters

The peak IVPD results for all three patient cohorts are plotted in Figure 3.5, the top plot. Both diseased patient cohorts displaying LV remodeling, DCM and LVH, show a decreased IVPD compared to the Normal patient cohort (Normal: 3.23 +/- 1.20 mmHg; LVH: 1.93 +/- 1.22 mmHg; versus DCM: 1.97 +/- 0.77 mmHg). Reported statistics are the group median and the inter-quartile range. IVPD shows statistical significance in distinguishing between the normal and the LVH cohort ($p = <0.0001$) and the DCM cohort ($p = 0.0003$), but is unable to differentiate between the two diseased cohorts ($p = 0.1896$). The conventional propagation velocity (V_P) measured by tracking the aliasing boundary iso-velocity contour as well as the V_S parameter were calculated. The patient cohort results for both of these parameters are also in Figure 3.5. Conventional V_P only shows statistical significance between the normal filling and hypertrophied cohorts ($p = 0.0056$) and V_S shows statistical significance between the normal filling and hypertrophied cohorts ($p < 0.0001$) and the normal and dilated cohorts ($p = 0.0335$). All group medians and interquartile ranges for the conventional parameters are summarized in Table 3.2.

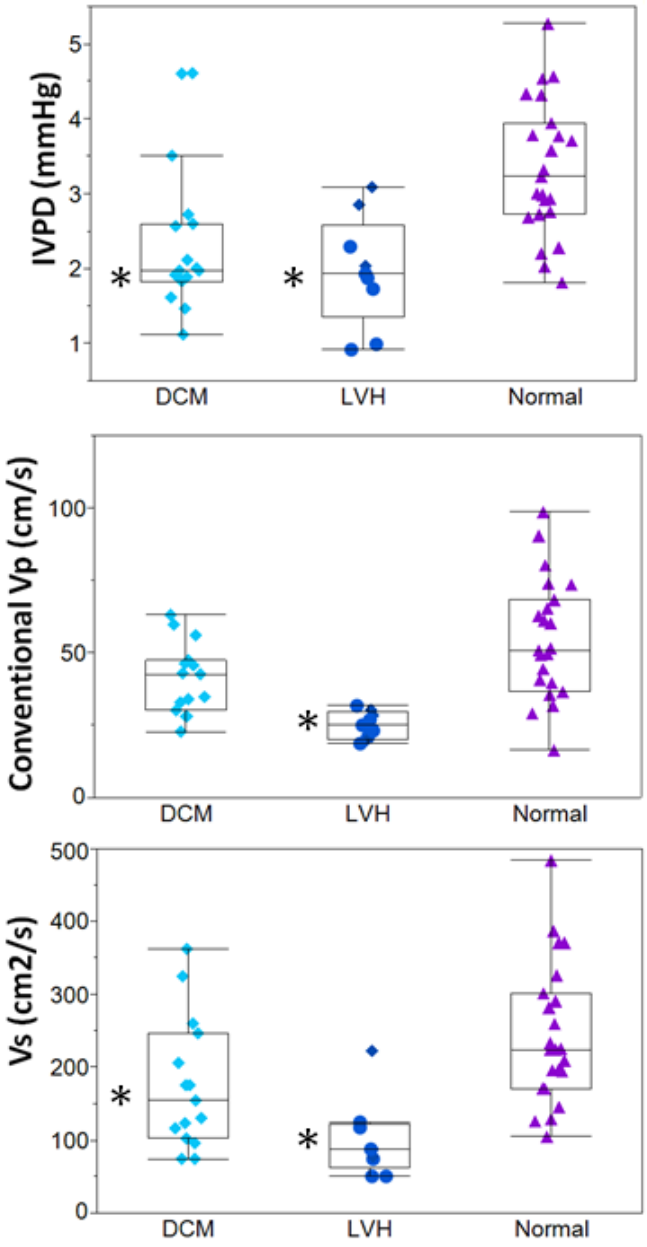

Figure 3.5: Conventional parameters for each patient cohort. Top, V_P Middle, V_S, Bottom, IVPD. Asterisks denote statistical significance.

Table 3.2: Summary of results for all three cohorts. Top table shows conventional parameters median and interquartile range. The bottom table shows the new CWT based parameters, dispersion rate, max wave component V_P and mean wave component V_P.

	IVPD		V_P		V_S	
	Median	IQR	Median	IQR	Median	IQR
Normal	3.23	1.20	50.62	31.84	224.12	130.75
LVH	1.93	1.22	24.84	9.06	87.00	58.82
DCM	1.97	0.77	42.59	17.28	154.38	144.14
	Dispersion Rate		Max wave V_P		Mean wave V_P	
	Median	IQR	Median	IQR	Median	IQR
Normal	266.26	249.61	49.69	23.11	27.71	11.20
LVH	111.88	172.17	23.39	19.94	15.98	12.59
DCM	32.04	142.20	21.98	11.67	12.97	9.28

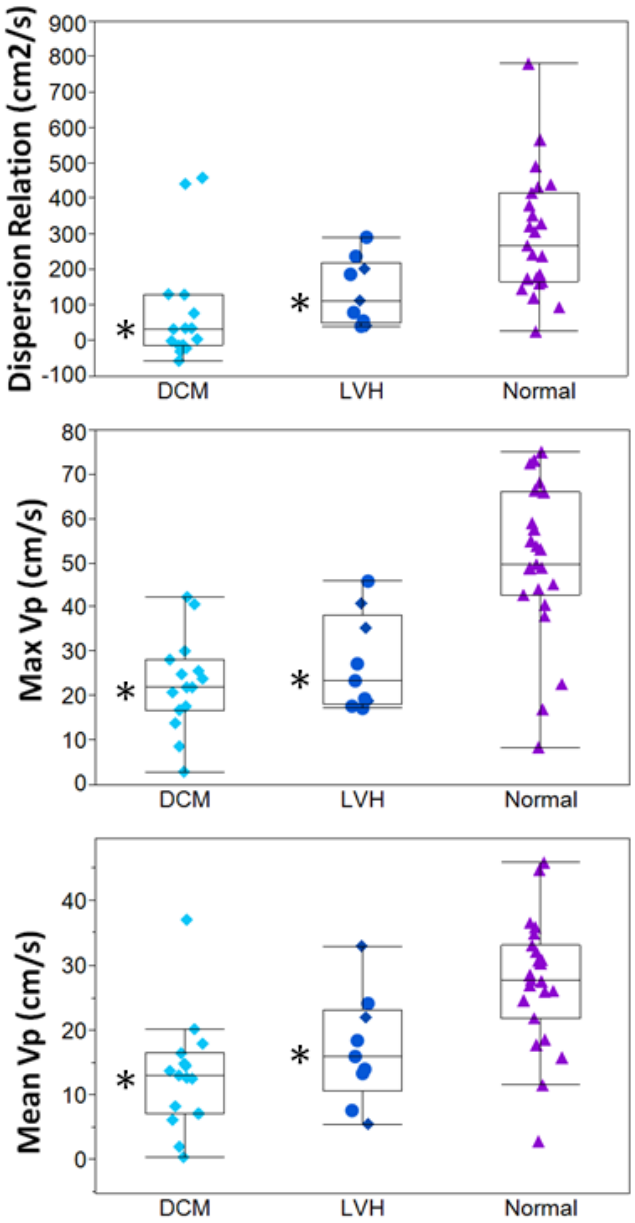

Figure 3.6: New parameters derived from the continuous wavelet transform algorithm. Top, dispersion rate, middle, maximum $V_{P,k}$ of all dominant wavenumbers, bottom, mean $V_{P,k}$ of all dominant wavenumbers. Asterisks denote statistical significance.

3.4.3 CWT Based Results

The dispersion rate, maximum wave component propagation velocity, and mean wave component propagation velocity were calculated for the full patient cohort and the results are plotted in Figure 3.6. In Figure 3.6 the dispersion rate plot reveals a reduced dispersion rate for the DCM cohort and a slightly reduced dispersion rate for the hypertrophied cohort when compared to the normal cohort (Normal: 266.26 +/- 249.61 cm^2/s, LVH: 111.88 +/- 172.17 cm^2/s, DCM: 32.04 +/- 142.2 cm^2/s). Reported statistics are the group median and the interquartile range. All three parameters show statistical significance when differentiating between the normal cohort and the DCM cohort (dispersion rate: $p < 0.004$; mean V_P: $p < 0.0001$; max V_P: $p < 0.0001$) and between the normal cohort and the LVH cohort (dispersion rate: $p < 0.0373$; mean V_P: $p < 0.0183$; max V_P: $p < 0.0006$, but none show statistical significance in differentiating between the two remodeled cohorts. The median values and interquartile ranges for all patient cohorts are summarized in Table 3.2.

The three new parameters based on the CWT analysis showed improved clinical utility over the conventional parameter V_P and the recently developed V_S as indicated by the increased area under the curve (AUC) on the receiver operator characteristic (ROC) curves plotted in Figure 3.7. The maximum wave component propagation velocity shows the highest AUC, followed closely by the Doppler-derived IVPD.

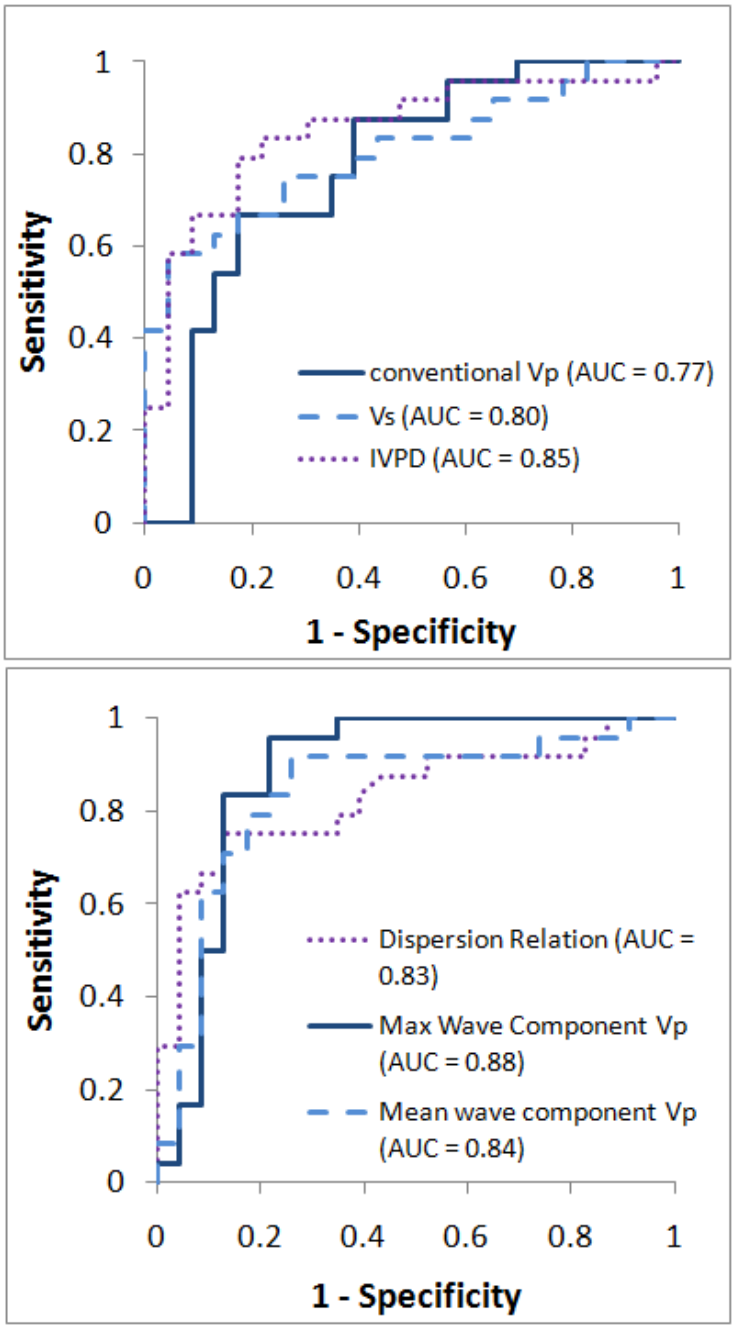

Figure 3.7: Operator Characteristic (ROC) curves for three conventional parameters (top) and for three proposed parameters (bottom). The area under the curve (AUC) is noted in the legend for each parameter. The maximum wave component V_P has the highest AUC of 0.88, but all three parameters on the left plot show improved AUC over the conventional V_P.

3.5 Discussion

3.5.1 Physical Significance of Dispersion Rate

The LV filling wave is dispersive because of the jet's viscous interactions with the myocardial wall. The mitral inflow jet interacts with the wall causing the wave to form smaller wave components which continue to propagate towards the apex at varying velocities. The shape of the ventricle will greatly affect how this jet interacts with the walls. An ideal elliptical shaped ventricle acts as a converging nozzle and preserves forward momentum towards the LV apex. A spherical ventricle may not be able to maintain this forward momentum and the filling may be inhibited due to convective deceleration of the flow. In addition to the walls interacting with the inflow jet and causing the formation of different wave components, the walls also act to constrain the mitral inflow jet and limit spreading away from the LV centerline. Dispersion is not detrimental to the filling process and may actually improve the efficiency of the early diastolic filling wave.

Previous work on radially confined vortex rings discovered a more rapid breakdown of vortex rings as the domain became more and more confined (*35*). The interaction between the vortex ring and the confinement wall causes the vortex rings to break down into smaller structures or waves. Although a dispersion rate was not quantified for this previous analysis, the physical mechanism causing the vortex ring breakdown in confined domains and the dispersive waves in the LV are similar.

In an elliptical LV, as blood flow crosses the mitral valve, the filling wave interacts with the myocardium. The elliptical geometry maintains forward momentum (towards the apex) and reduces convective spreading. In doing this, the myocardium causes the filling wave to break down into smaller structures or waves which will continue to propagate at different velocities. This phenomenon is captured in the dispersion rate parameter measured above.

3.5.2 Discussion of Representative Patients

The dispersion rate was calculated for the three cohorts consisting of patients with normal filling, hypertrophied ventricles and dilated ventricles shows significant changes in the wave as the LV remodels in response to disease. The normal patients have elliptical shaped ventricles, forming a converging geometry which constrains the expansion of the mitral inflow jet, better preserves the momentum towards the apex. Normal ventricles are capable of generating a sufficient pressure gradient across the mitral valve for the LV to fill without an increase in left atrial pressure. In heart disease, the myocardium remodels in response to increased loading conditions and this elliptical geometry is lost. The remodeling process is not completely understood. Many cell signaling pathways are altered as the disease progresses and are the most likely cause for this change in LV remodeling. These factors are beyond the scope of this paper, but are well detailed in (*7, 36, 37*).

Left ventricular hypertrophy (LVH) typically occurs in response to increased pressure loading on the heart (*38*), and may also be present in some wall regions after infarction (*39*). Due to the increased wall thickness, stiffness, and other mechanisms associated with the specific disease, the hypertrophied LV is unable to generate suction to drive the filling wave (*2*). The narrowed LV chamber still acts to constrain the flow and causes the filling wave to spread towards the apex, similar to the normal elliptical LVs but to a lesser degree. The smaller dispersion could be due to a simultaneous loss of suction, evident by the reduced IVPD (Figure 3.5).

The dilated LV may be a result of myocardial infarct, or due to volume overload which causes the myocytes to lengthen and the myocardium to stretch (*40*). The dilated LV becomes spherical and is unable to generate suction due to reduced wall motion and other mechanisms related with the specific disease (*16*). Due to the spherical shape, the dilated LV is unable to constrain the LV filling wave to disperse towards the apex. In this state, the filling wave is a bulk flow wave with increased spreading of the mitral inflow jet away from the LV centerline.

3.5.3 Dispersion Rate and Individual Component Propagation Velocity

The dispersion rate analysis applied to the three patient cohorts is able to distinguish between the normal LVs and the remodeled LVs Figure 3.6). Also the improved area under the ROC curves in Figure 3.7 and Table 3.2 show improved clinical utility of the dispersion rate over conventional Doppler parameters (Vp, Vs, IVPD). This parameter may act as an improved diagnostic tool which is able to better describe the physical process and the mechanisms that govern LV filling, while differentiating between health and disease.

This CWT analysis is also valuable because it gives a more detailed view of the propagation velocity of the wave. We are now capable of measuring the propagation velocity of each individual wave component. The propagation velocity of the individual components could provide an improved diagnostic parameter to replace conventional propagation velocity. In this work, both the maximum propagation velocity of all wave components and the mean propagation velocity of all dominant wave components were investigated. Both the maximum wave component velocity and the mean wave component velocity show improved clinical utility (Figure 3.7) over both the dispersion rate and the conventional parameters. This implies that by analyzing individual wave component propagation velocities, and not just tracking one iso-velocity contour, we can develop a better understanding and classification process for LVDD.

3.5.4 Limitations and Non-Monotonicity

The dispersion rate values reported in Figure 3.6 and Table 3.2 are calculated by fitting a line to the dominant wavenumbers in the signal. These relationships are typically linear. However, the full spectrum of propagation velocities for all wavenumbers is not necessarily linear. This relationship can be linear, but can also be non-monotonic as it was observed in many of the CMM echocardiograms analyzed. Common behaviors included a “plateau”, where the propagation velocities would increase to a certain value and then level off and remain relatively constant. Another common behavior was a “peak”, where the propagation velocities would increase, reach a peak, and then begin decreasing with increasing wavenumber. The physical significance

of these non-monotonic trends that were observed is not fully understood and will be the subject of future work. It is possible that these different trends represent various mixing patterns within the LV. As flow interacts with the walls and is redirected through the LV, different groups of wave components may move together at varying velocities. Several examples of these two trends are plotted in Figure 3.8.

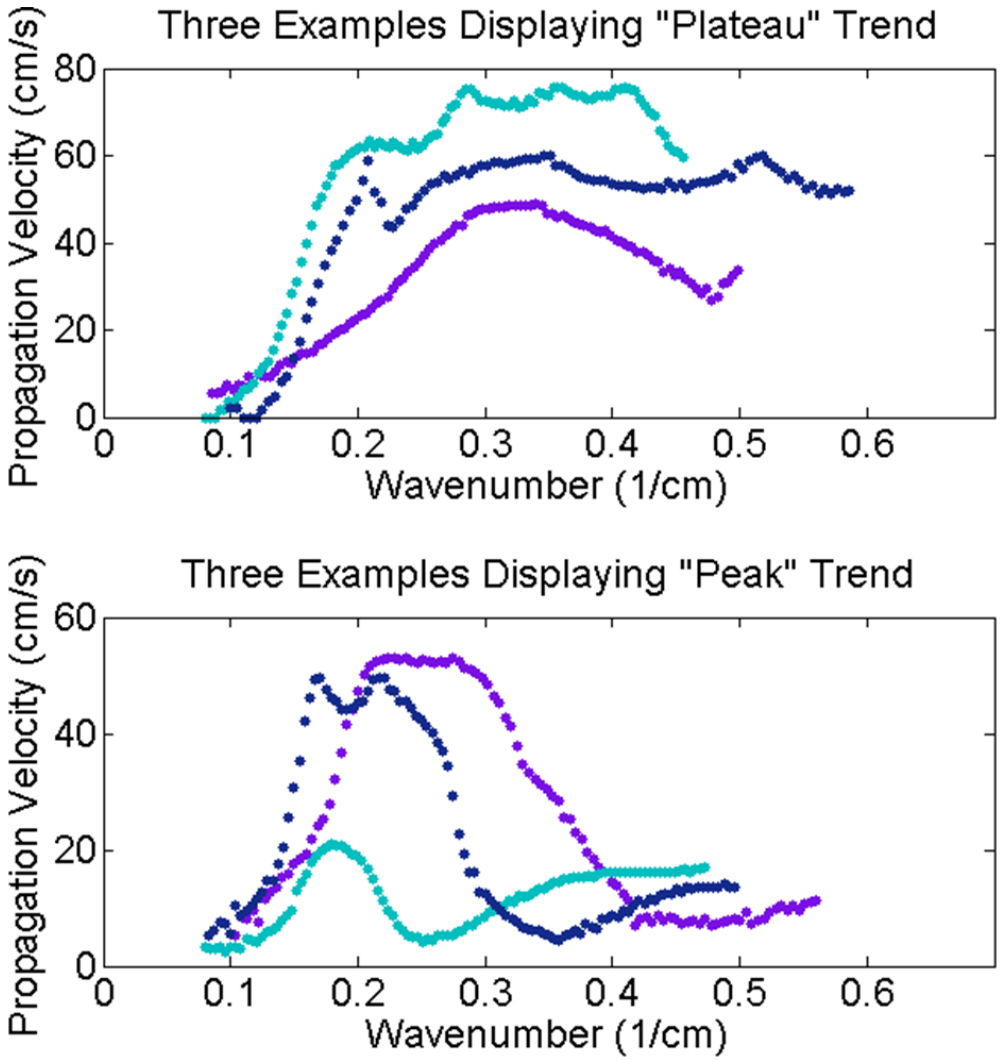

Figure 3.8: Non-monotonic trends in dispersion relation curves. Top plot shows three example patients displaying a plateau trend where the curve increases fairly linearly and then reaches a plateau value. The bottom plot shows three example patients displaying a peak trend, where the curve increases fairly linearly, reaches a peak, and then decreases again.

3.6 Conclusions

We discovered that LV filling waves are dispersive and the degree of dispersion can vary with progressing disease states. The dispersion rate is dependent on the geometry of the LV, and is capable of distinguishing between normal filling and two remodeled LV geometries, dilated cardiomyopathy and left ventricular hypertrophy, helping us gain a more physical understanding of the interactions between wall geometry, pressure gradients, and LV filling waves. This analysis also gives the capability to analyze individual wave component propagation velocities, offering more insight to the dynamics of the LV filling waves and potentially improving clinical utility of Doppler-derived diagnostic parameters.

3.7 References

1. L. H. Opie, *The heart : physiology, from cell to circulation*. (Lippincott-Raven, Philadelphia, 1998).
2. R. A. O'Rourke. (McGraw-Hill Medical Pub. Division, New York, 2001).
3. M. R. Zile, D. L. Brutsaert, New concepts in diastolic dysfunction and diastolic heart failure: Part I Diagnosis, prognosis, and measurements of diastolic function. *Circulation* **105**, 1387 (Mar, 2002).
4. W. J. Paulus *et al.*, How to diagnose diastolic heart failure: a consensus statement on the diagnosis of heart failure with normal left ventricular ejection fraction by the Heart Failure and Echocardiography Associations of the European Society of Cardiology. *Eur. Heart J.* **28**, 2539 (Oct, 2007).
5. T. Kuznetsova, L. Herbots, Y. Jin, K. Stolarz-Skrzypek, J. A. Staessen, Systolic and diastolic left ventricular dysfunction: from risk factors to overt heart failure. *Expert Rev Cardiovasc Ther* **8**, 251 (2010).
6. R. L. Shammas, N. U. Khan, R. Nekkanti, A. Movahed, Diastolic heart failure and left ventricular diastolic dysfunction: what we know, and what we don't know! *Int J Cardiol* **115**, 284 (2007).
7. L. H. Opie, P. J. Commerford, B. J. Gersh, M. A. Pfeffer, Controversies in ventricular remodelling. *Lancet* **367**, 356 (2006).
8. S. F. Nagueh *et al.*, Recommendations for the Evaluation of Left Ventricular Diastolic Function by Echocardiography. *Eur. J. Echocardiogr.* **10**, 165 (Mar, 2009).
9. M. W. Sessoms, J. Lisauskas, S. J. Kovacs, The left ventricular color M-mode Doppler flow propagation velocity V(p): in vivo comparison of alternative

methods including physiologic implications. *J Am Soc Echocardiogr* **15**, 339 (2002).

10. K. C. Stewart *et al.*, Evaluation of LV Diastolic Function From Color M-Mode Echocardiography. *JACC: Cardiovascular Imaging* **4**, 37 (2011).
11. P. Brun *et al.*, LEFT-VENTRICULAR FLOW PROPAGATION DURING EARLY FILLING IS RELATED TO WALL RELAXATION - A COLOR M-MODE DOPPLER ANALYSIS. *J. Am. Coll. Cardiol.* **20**, 420 (Aug, 1992).
12. M. Stugaard, C. Risoe, H. Ihlen, O. A. Smiseth, INTRACAVITARY FILLING PATTERN IN THE FAILING LEFT-VENTRICLE ASSESSED BY COLOR M-MODE DOPPLER-ECHOCARDIOGRAPHY. *J. Am. Coll. Cardiol.* **24**, 663 (Sep, 1994).
13. Y. Seo *et al.*, Assessment of propagation velocity by contrast echocardiography for standardization of color Doppler propagation velocity measurements. *J Am Soc Echocardiogr* **17**, 1266 (2004).
14. M. W. Sessoms, J. Lisauskas, S. J. Kovacs, The left ventricular color M-mode Doppler flow propagation velocity V-p: In vivo comparison of alternative methods including physiologic implications. *Journal of the American Society of Echocardiography* **15**, 339 (Apr, 2002).
15. A. Hirose, K. E. Lonngren, *Introduction to wave phenomena*. (Wiley, New York, 1985).
16. R. Yotti *et al.*, A noninvasive method for assessing impaired diastolic suction in patients with dilated cardiomyopathy. *Circulation* **112**, 2921 (Nov, 2005).
17. J. N. Chapman, J. Mayet, R. A. Foale, S. A. Thom, Intraventricular dispersion of E wave velocity: an alternative measure of left ventricular diastolic function in hypertensive patients? *J. Hum. Hypertens.* **13**, 867 (Dec, 1999).
18. O. Kozan *et al.*, Use of intraventricular dispersion of the peak diastolic flow velocity as a marker of left ventricular diastolic dysfunction in patients with atrial fibrillation. *J Am Soc Echocardiogr* **11**, 1036 (1998).
19. F. Canturk *et al.*, Combined use of propagation velocity and intraventricular dispersion of E wave velocity for the evaluation of diastolic functions in patients with rheumatoid arthritis. *Int J Cardiovasc Imaging* **22**, 369 (2006).
20. R. M. Lang *et al.*, Recommendations for Chamber Quantification: A Report from the American Society of Echocardiography's Guidelines and Standards Committee and the Chamber Quantification Writing Group, Developed in Conjunction with the European Association of Echocardiography, a Branch of the European Society of Cardiology. *Journal of the American Society of Echocardiography* **18**, 1440 (2005).
21. J. Madaric *et al.*, Early and late effects of cardiac resynchronization therapy on exercise-induced mitral regurgitation: relationship with left ventricular dyssynchrony, remodelling and cardiopulmonary performance. *Eur Heart J* **28**, 2134 (2007).

22. A. Aldroubi, M. A. Unser, *Wavelets in medicine and biology*. (CRC Press, Boca Raton, 1996).

23. P. S. Addison, *The illustrated wavelet transform handbook : introductory theory and applications in science, engineering, medicine, and finance*. (Institute of Physics Pub., Bristol, UK; Philadelphia, 2002).

24. J. Lin, L. Qu, FEATURE EXTRACTION BASED ON MORLET WAVELET AND ITS APPLICATION FOR MECHANICAL FAULT DIAGNOSIS. *Journal of sound and vibration* **234**, 135 (2000).

25. G. Berkooz, The Proper Orthogonal Decomposition in the Analysis of Turbulent Flows. *Annu. Rev. Fluid Mech.* **25**, 539 (1993).

26. T. R. Smith, Low-Dimensional Modelling of Turbulence Using the Proper Orthogonal Decomposition: A Tutorial. *Nonlinear dynamics* **41**, 275 (2005).

27. N. Aubry, Spatiotemporal analysis of complex signals: Theory and applications. *Journal of statistical physics* **64**, 683 (1991).

28. W. A. Taylor. (2000), vol. 2008.

29. N. L. Greenberg, P. M. Vandervoort, J. D. Thomas, Instantaneous diastolic transmitral pressure differences from color Doppler M mode echocardiography. *Am. J. Physiol.-Heart Circul. Physiol.* **271**, H1267 (Oct, 1996).

30. N. L. Greenberg, P. M. Vandervoort, M. S. Firstenberg, M. J. Garcia, J. D. Thomas, Estimation of diastolic intraventricular pressure gradients by Doppler M-mode echocardiography. *Am. J. Physiol.-Heart Circul. Physiol.* **280**, H2507 (Jun, 2001).

31. A. Rovner *et al.*, Improvement in diastolic intraventricular pressure gradients in patients with HOCM after ethanol septal reduction. *American Journal of Physiology - Heart and Circulatory Physiology* **285**, H2492 (December 1, 2003, 2003).

32. S. F. Nagueh *et al.*, Recommendations for the Evaluation of Left Ventricular Diastolic Function by Echocardiography. *Eur. J. Echocardiogr.* **10**, 165 (March 1, 2009, 2009).

33. R. D. Mosteller, Simplified calculation of body-surface area. *The New England journal of medicine* **317**, 1098 (1987).

34. R. B. Devereux *et al.*, Echocardiographic assessment of left ventricular hypertrophy: Comparison to necropsy findings. *The American Journal of Cardiology* **57**, 450 (1986).

35. K. C. Stewart, J. C. Charonko, C. L. Niebel, W. C. Little, P. P. Vlachos, Left ventricle filling vortex formation is unaffected by diastolic impairment. *American Journal of Physiology - Heart and Circulatory Physiology*, (September 7, 2012, 2012).

36. M. R. Zile, D. L. Brutsaert, New concepts in diastolic dysfunction and diastolic heart failure: Part II - Causal mechanisms and treatment. *Circulation* **105**, 1503 (Mar, 2002).

37. M. A. Konstam, D. G. Kramer, A. R. Patel, M. S. Maron, J. E. Udelson, Left ventricular remodeling in heart failure: current concepts in clinical significance and assessment. *JACC Cardiovasc Imaging* **4**, 98 (2011).

38. F. Z. MEERSON, Compensatory Hyperfunction of the Heart and Cardiac Insufficiency. *Circ.Res.* **10**, 250 (March 1, 1962, 1962).

39. M. G. S. J. Sutton, N. Sharpe, Left Ventricular Remodeling After Myocardial Infarction : Pathophysiology and Therapy. *Circulation* **101**, 2981 (June 27, 2000, 2000).

40. W. Grossman, Wall stress and patterns of hypertrophy in the human left ventricle. *The Journal of clinical investigation* **56**, 56 (1975).

4. Conclusions and Future Work

4.1 Dispersion Rate

This work has made strides in moving towards an improved physical understanding of diastole and has also developed new methodologies to quantify LV filling waves. The main contribution of this work is the discovery that LV filling waves move as dispersive waves as opposed to bulk flow waves as was previously assumed. The physical and clinical implications of this discovery are also investigated and further discussed. Physically this finding presents a link between the filling wave dynamics and LV geometry and suggests how the filling wave may be affected by various disease states. Clinically, this could lead to improved diagnostics based on a true understanding of the wave motion and by eliminating all prior assumptions based on iso-velocity contours in quantifying the wave motion.

The present algorithm has many complicated signal processing steps and much room for improvement. The future work for algorithm improvement is listed below, as well as future work for expanding this dispersion relation analysis.

4.1.2 Algorithm Improvements

- Quantify the effects of wavelet parameters f_o and f_b. This could be done by a direct comparison between the CWT power spectra, and also by comparing which wavenumbers each mother wavelet and scaling function identifies as a dominant wavenumber.
- Quantify the effect of varying the POD cutoff mode (right now it is determined based on POD mode entropy) on the estimation of signal to noise. Determine if this is the best method to obtain an initial estimate of signal and noise.

- Determine if there are better options for optimizing a cutoff frequency than the application of a pseudo Gaussian filter.
- Analyze the effect of including more or less oscillations in the mother wavelet. Right now six is used; due to a recommended range of 5-7.
- To determine the dominant wavenumbers at which to calculate the dispersion rate, right now the relative energy that each wavenumber is contributing to the total CWT spectra is calculated and the wavenumber at which this spectrum falls below 10% is the maximum wavenumber considered. This parameter should also be optimized.
- Determine the best method for tracking the motion of the frequency components between time t1 and time t2. Right now, the peaks are simply identified. A cross correlation should also be investigated.
- Currently the dispersion rate is calculated between two median power spectra, one near the beginning of the filling wave and one near the end. It may be useful to track the peak motion of each wavenumber continuously at each time step on the CMM echocardiogram.
- Determine the best method for quantifying the dispersion relationship if the relation between wavenumber and propagation velocity is not linear.

4.1.3 Dispersion Rate Future Work

- It would be interesting to apply this algorithm to a 2D or 3D velocity field to quantify the dispersion in multiple dimensions.
- Also, the dispersion rate could be applied to a series of confined and unconfined vortex rings generated in a piston cylinder device. It would be beneficial to see how the dispersion rate changes during periods of vortex ring break down.
- Apply the mean wave component V_P and the max wave component V_P analysis to a larger patient cohort at all stages of LVDD.

4.2 CMM Reconstruction

The second manuscript presents a new methodology to improve Doppler-derived IVPD measurements from CMM echocardiography. It was found that the Doppler-derived IVPD is highly dependent on the scanner sweep speed. Due to low sampling, many events in the filling process, such as time of peak IVPD, could be missed on the recorded scan. A new methodology using a spatio-temporal POD reconstruction to a higher temporal resolution can rectify the CMM echocardiograms so that all scans are at a uniform temporal resolution. This removes any effects from scanner settings and improves IVPD estimation.

This algorithm also presents a new method of generating a single representative beat. This beat takes into account common information from a series of heartbeats and eliminates non-similar information. This allows reconstruction of a representative heartbeat at an improved temporal resolution, eliminating misleading IVPD measurements due to beat-to-beat variations.

4.2.1 CMM Reconstruction Future Work

- Obtain invasive catheter measurements and simultaneous CMM echocardiography in a canine or porcine model. Use this data to validate current methodology to show that the high resolution reconstructed scans are returning more accurate and physiological IVPD values.
- Improve beat alignment when performing the representative beat reconstruction. Odd beats, or patients with inconsistent heart rate should not be used.
- Determine an optimal resolution to reconstruct to. Determine if this resolution exists or will it vary patient to patient.
- Apply this algorithm to all clinical data, including MRI and echoPIV which are notoriously recorded at lowered resolutions.

Appendix A

Proper Orthogonal Decomposition

Proper Orthogonal Decomposition (POD) is a signal processing technique commonly used in engineering to decompose a signal into a series of modes or basis functions. POD does not require any a priori knowledge of the signal basis functions as the basis functions are determined based on an energetically optimal reduction of the signal into its fundamental modes. Given a velocity signal U(x,t), POD finds an optimal basis function φ that maximizes the relationship shown in Equation A-1, where $\langle \cdot \rangle$ is the ensemble average and $(\cdot,\cdot)$ is the inner product.

$$max \frac{\langle (U,\varphi)^2 \rangle}{(\varphi,\varphi)} \qquad \textbf{A-1}$$

Essentially, POD acts to maximize the projection of the velocity field onto the basis function so that the maximum energy is captured by that particular basis function. The actual basis functions are found by solving the Fredholm equation which is detailed in (*1*). This solution results in a series of orthogonal eigenfunctions, the known energy each function contributes to the original signal, and corresponding temporal mode coefficients. The original signal can be recovered as shown in Equation A-2 where a_i are the temporal mode coefficients and φ_i are the eigenfunctions.

.

$$U(x,t) = \sum_{i=1}^{K} a_i(t)\varphi_i(x) \qquad \textbf{A-2}$$

The energy of each mode, λ_i, is another result of the Fredholm equation. The relative mode energy is defined in Equation A-3.

$$Energy_{relative} = \frac{\lambda_i}{\sum_{j=1}^{\infty} \lambda_j} \quad \textbf{A-3}$$

The initial basis functions capture most of the energy in the original signal and the final basis functions most likely capture noise and irregularities in the signal. By reconstructing the signal using a subset of the basis functions, a reconstructed signal with all of the dominant features of the signal, but without the noise can be recovered.

References

1. T. R. Smith, Low-Dimensional Modelling of Turbulence Using the Proper Orthogonal Decomposition: A Tutorial. *Nonlinear dynamics* **41**, 275 (2005).

Appendix B

The Continuous Wavelet Transform

The continuous wavelet transform (CWT) acts as a varying bandwidth band pass filter by convolving an original signal with a series of scaled and translated continuous wavelet functions (*1-3*). It is an improvement upon Fourier methods as it provides spatially localized frequency information whereas Fourier methods only reveal the present frequency components as shown in Figure B-1. The scaling parameter gives frequency localization while the translation parameter gives spatial or temporal localization. The CWT has been used in countless applications across all engineering disciplines (*4-8*) and gives the energy of the signal localized in space, time, and frequency.

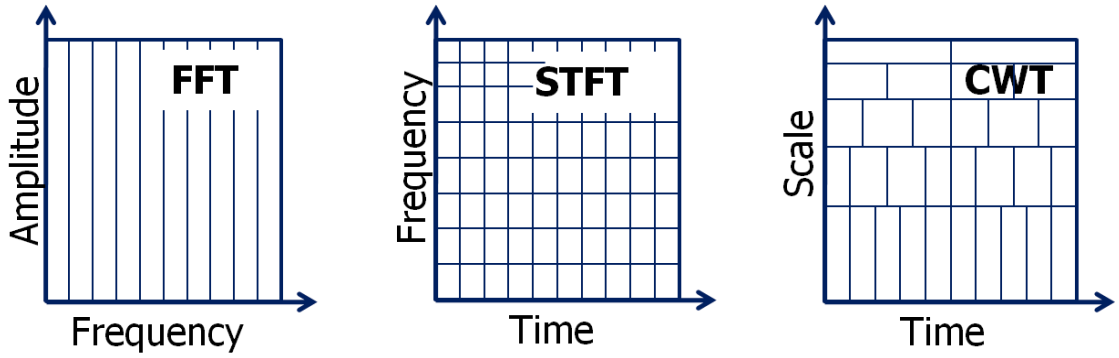

Figure B-1: The Fourier transform (FFT) only reveals what frequency components are present in a signal. The short time Fourier transform reveals some temporal localization, but there are issues with choosing an appropriate resolution to capture both high frequency components and low frequency components. The Continuous Wavelet Transform (CWT) using scaled and translated wavelet functions to give temporal localization as well as to enable "zooming in or out" to always have the appropriate resolution to capture high and/or low frequency components.

In this work, the CWT is applied in MATLAB, and is a convolution of the original signal and the series of scaled and translated wavelet functions, yielding a three dimensional map of the CMM signal energy in spatial location, spatial frequency, and CMM time step as shown in Equation B-1, where a is the scaling parameter, b is the translation parameter, f(x) is the signal being analyzed and $\psi(\frac{x-b}{a})$ is one of a series of continuous wavelet functions.

$$W_T = \frac{1}{a}\int f(x) * \psi\left(\frac{x-b}{a}\right)dt \qquad \textbf{B-1}$$

A wavelet function is any continuous function with zero mean and zero magnitude at the end points. The scaling (stretching or compressing) gives frequency localization. The mother wavelet is scaled using a user defined scaling function a. The scaling of the mother wavelet is inversely proportional to the frequency of the resulting wavelet as defined in Equation B- 2, where f_o is the center frequency of the wavelet and delta t is the resolution of the original signal.

$$\omega = \frac{f_o}{a\Delta x} \qquad \textbf{B- 2}$$

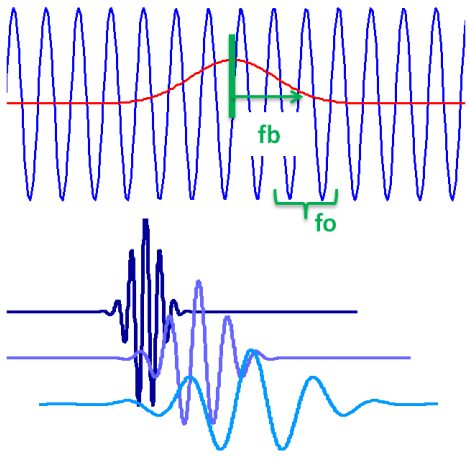

Figure B-2: Top, a Morlet wavelet is essentially a sine wave modulated by a Gaussian impulse. Bottom: Morlet wavelets at several scales and translations.

The complex Morlet wavelet, Equation B- 3 has been used across a wide range of applications, but has been found especially useful when analyzing biological signals (*9-11*). The smooth oscillations and high control over resulting frequency spectrum make this a valuable wavelet in biological applications and therefore it was chosen for this analysis. A complex Morlet wavelet is a plane wave (frequency fo) modulated by a Gaussian function (bandwidth fb) as shown in Figure B-2. By altering these two parameters, any number of mother wavelets can be generated. Two conditions are that the wavelet maintains zero mean and that the endpoints have zero magnitude (*12*).

$$\Psi(x) = \frac{1}{\sqrt{\pi f_b}} e^{i2\pi f_o x} e^{-\frac{x^2}{f_b}} \qquad \text{B- 3}$$

It is also important to define an appropriate range of scales at which to stretch and or compress the mother wavelet so that the resulting wavelet functions are relevant to your application.

The choice of mother wavelet has been found to greatly affect the resulting CWT power spectra. For this reason, it is very important to choose an appropriate mother

wavelet which is best for analyzing the signal of interest (*13*). The two tuning parameters, fo and fb, control the total number of oscillations in the mother wavelet. A total number of five to seven oscillations is recommended to ensure zero mean (*12*). The relationship between the two parameters and the number of cycles is defined in Equation B-4. Either f_b or f_o can be optimized and the other parameter can then be solved for using this relationship.

$$f_b = \frac{n_{cycles}}{2\pi f_o} \qquad \text{B-4}$$

References

1. C. Torrence, G. P. Compo, A Practical Guide to Wavelet Analysis. *Bulletin of the American Meteorological Society* **79**, 61 (1998/01/01, 1998).
2. P. S. Addison, *The illustrated wavelet transform handbook : introductory theory and applications in science, engineering, medicine, and finance*. (Institute of Physics Pub., Bristol, UK; Philadelphia, 2002).
3. I. Daubechies, The wavelet transform, time-frequency localization and signal analysis. *Information Theory, IEEE Transactions on* **36**, 961 (1990).
4. Z. K. Peng, F. L. Chu, Application of the wavelet transform in machine condition monitoring and fault diagnostics: a review with bibliography. *Mechanical Systems and Signal Processing* **18**, 199 (2004).
5. W. M. Briggs, R. A. Levine, Wavelets and Field Forecast Verification. *Monthly Weather Review* **125**, 1329 (1997/06/01, 1997).
6. A. Grinsted, Moore, J.C., Jevrejeva, S. , Application of the cross wavelet transform and wavelet coherence to geophysical time series. *Nonlin.Processes Geophys.* **11**, 561 (2004/11/18, 2004).
7. P. He, P. Li, H. Sun, Feature Extraction of Acoustic Signals Based on Complex Morlet Wavelet. *Procedia Engineering* **15**, 464 (2011).
8. Y. Jiang, B. Tang, Y. Qin, W. Liu, Feature extraction method of wind turbine based on adaptive Morlet wavelet and SVD. *Renewable Energy* **36**, 2146 (2011).
9. B. J. Roach, D. H. Mathalon, Event-Related EEG Time-Frequency Analysis: An Overview of Measures and An Analysis of Early Gamma Band Phase Locking in Schizophrenia. *Schizophrenia Bulletin* **34**, 907 (September 1, 2008, 2008).
10. M. Akay, Wavelet applications in medicine. *Spectrum, IEEE* **34**, 50 (1997).
11. A. Aldroubi, M. A. Unser, *Wavelets in medicine and biology*. (CRC Press, Boca Raton, 1996).
12. D. Morlet, F. Peyrin, P. Desseigne, P. Touboul, P. Rubel, WAVELET ANALYSIS OF HIGH-RESOLUTION SIGNAL-AVERAGED ECGS IN

POSTINFARCTION PATIENTS. *Journal of Electrocardiology* **26**, 311 (Oct, 1993).

13. G. Meng, K. Kageyama, Z. Su, L. Ye, Optimal Mother Wavelet Selection for Lamb Wave Analyses. *Journal of intelligent material systems and structures* **20**, 1147 (2009).

Appendix C

IRB Approval Letters

VirginiaTech

Office of Research Compliance
Institutional Review Board
2000 Kraft Drive, Suite 2000 (0497)
Blacksburg, Virginia 24060
540/231-4606 Fax 540/231-0959
e-mail irb@vt.edu
Website: www.irb.vt.edu

MEMORANDUM

DATE: August 24, 2011

TO: Pavlos P. Vlachos, Kelley Stewart, John Charonko, Casandra Niebel, Ashley Gregory, Robert Decarolis

FROM: Virginia Tech Institutional Review Board (FWA00000572, expires May 31, 2014)

PROTOCOL TITLE: Translational Science Team Pilot Application: Left Ventricle Filling Hydrodynamic Efficiency and Pressure Distributions as a Predictive Tool for Diagnosing Cardiac Diastolic Dysfunction

IRB NUMBER: 08-057

Effective August 23, 2011, the Virginia Tech IRB Chair, Dr. David M. Moore, approved the amendment request for the above-mentioned research protocol.

This approval provides permission to begin the human subject activities outlined in the IRB-approved protocol and supporting documents.

Plans to deviate from the approved protocol and/or supporting documents must be submitted to the IRB as an amendment request and approved by the IRB prior to the implementation of any changes, regardless of how minor, except where necessary to eliminate apparent immediate hazards to the subjects. Report promptly to the IRB any injuries or other unanticipated or adverse events involving risks or harms to human research subjects or others.

All investigators (listed above) are required to comply with the researcher requirements outlined at http://www.irb.vt.edu/pages/responsibilities.htm (please review before the commencement of your research).

PROTOCOL INFORMATION:
Approved as: **Expedited, under 45 CFR 46.110 category(ies) 5**
Protocol Approval Date: **2/13/2011 (protocol's initial approval date: 2/13/2008)**
Protocol Expiration Date: **2/12/2012**
Continuing Review Due Date*: **1/29/2012**
*Date a Continuing Review application is due to the IRB office if human subject activities covered under this protocol, including data analysis, are to continue beyond the Protocol Expiration Date.

FEDERALLY FUNDED RESEARCH REQUIREMENTS:
Per federally regulations, 45 CFR 46.103(f), the IRB is required to compare all federally funded grant proposals / work statements to the IRB protocol(s) which cover the human research activities included in the proposal / work statement before funds are released. Note that this requirement does not apply to Exempt and Interim IRB protocols, or grants for which VT is not the primary awardee.

The table on the following page indicates whether grant proposals are related to this IRB protocol, and which of the listed proposals, if any, have been compared to this IRB protocol, if required.

VirginiaTech

Office of Research Compliance
Institutional Review Board
2000 Kraft Drive, Suite 2000 (0497)
Blacksburg, Virginia 24060
540/231-4606 Fax 540/231-0959
e-mail irb@vt.edu
Website: www.irb.vt.edu

MEMORANDUM

DATE: January 17, 2012

TO: Pavlos P. Vlachos, Kelley Stewart, John Charonko, Casandra Niebel, Brett Meyers, Robert Decarolis

FROM: Virginia Tech Institutional Review Board (FWA00000572, expires May 31, 2014)

PROTOCOL TITLE: Translational Science Team Pilot Application: Left Ventricle Filling Hydrodynamic Efficiency and Pressure Distributions as a Predictive Tool for Diagnosing Cardiac Diastolic Dysfunction

IRB NUMBER: 08-057

Effective February 13, 2012, the Virginia Tech IRB Chair, Dr. David M. Moore, approved the continuation request for the above-mentioned research protocol.

This approval provides permission to begin the human subject activities outlined in the IRB-approved protocol and supporting documents.

Plans to deviate from the approved protocol and/or supporting documents must be submitted to the IRB as an amendment request and approved by the IRB prior to the implementation of any changes, regardless of how minor, except where necessary to eliminate apparent immediate hazards to the subjects. Report promptly to the IRB any injuries or other unanticipated or adverse events involving risks or harms to human research subjects or others.

All investigators (listed above) are required to comply with the researcher requirements outlined at http://www.irb.vt.edu/pages/responsibilities.htm (please review before the commencement of your research).

PROTOCOL INFORMATION:
Approved as: **Expedited, under 45 CFR 46.110 category(ies) 5**
Protocol Approval Date: **2/13/2012 (protocol's initial approval date: 2/13/2008)**
Protocol Expiration Date: **2/12/2013**
Continuing Review Due Date*: **1/29/2013**
*Date a Continuing Review application is due to the IRB office if human subject activities covered under this protocol, including data analysis, are to continue beyond the Protocol Expiration Date.

FEDERALLY FUNDED RESEARCH REQUIREMENTS:
Per federally regulations, 45 CFR 46.103(f), the IRB is required to compare all federally funded grant proposals / work statements to the IRB protocol(s) which cover the human research activities included in the proposal / work statement before funds are released. Note that this requirement does not apply to Exempt and Interim IRB protocols, or grants for which VT is not the primary awardee.

The table on the following page indicates whether grant proposals are related to this IRB protocol, and which of the listed proposals, if any, have been compared to this IRB protocol, if required.